Journal of
Marine Science and Engineering

MDPI

Article

Artificial Intelligence for Computational Remote Sensing: Quantifying Patterns of Land Cover Types around Cheetham Wetlands, Port Phillip Bay, Australia

Polina Lemenkova [1,2]

[1] Department of Geoinformatics, Faculty of Digital and Analytical Sciences, Paris Lodron Universität Salzburg, Schillerstraße 30, A-5020 Salzburg, Austria; polina.lemenkova@plus.ac.at or polina.lemenkova2@unibo.it; Tel.: +43-677-6173-2772 or +39-344-69-28-732

[2] Department of Biological, Geological and Environmental Sciences, Alma Mater Studiorum—Università di Bologna, Via Irnerio 42, 40126 Bologna, Italy

Abstract: This paper evaluates the potential of using artificial intelligence (AI) and machine learning (ML) approaches for classification of Landsat satellite imagery for environmental coastal mapping. The aim is to identify changes in patterns of land cover types in a coastal area around Cheetham Wetlands, Port Phillip Bay, Australia. The scripting approach of the Geographic Resources Analysis Support System (GRASS) geographic information system (GIS) uses AI-based methods of image analysis to accurately discriminate land cover types. Four ML algorithms are applied, tested and compared for supervised classification. Technical approaches are based on using the 'r.learn.train' module, which employs the scikit-learn library of Python. The methodology includes the following algorithms: (1) random forest (RF), (2) support vector machine (SVM), (3) an ANN-based approach using a multi-layer perceptron (MLP) classifier, and (4) a decision tree classifier (DTC). The tested methods using AI demonstrated robust results for image classification, with the highest overall accuracy exceeding 98% and reached by the SVM and RF models. The presented scripting approach for GRASS GIS accurately detected changes in land cover types in southern Victoria over the period of 2013–2024. From our findings, the use of AI and ML algorithms offers effective solutions for coastal monitoring by analysis of change detection using multi-temporal RS data. The demonstrated methods have potential applications in coastal and wetland monitoring, environmental analysis and urban planning based on Earth observation data.

Keywords: image processing; Earth observation; coasts; GIS; cartography; geoinformatics; landscape analysis; environmental monitoring; sensors; machine learning; Melbourne; Victoria

check for updates

Citation: Lemenkova, P. Artificial Intelligence for Computational Remote Sensing: Quantifying Patterns of Land Cover Types around Cheetham Wetlands, Port Phillip Bay, Australia. *J. Mar. Sci. Eng.* **2024**, *12*, 1279. https://doi.org/10.3390/jmse12081279

Academic Editors: Po Hu, Yuanzhi Zhang, Lin Li and Dongmei Chen

Received: 27 June 2024
Revised: 18 July 2024
Accepted: 28 July 2024
Published: 29 July 2024

Copyright: © 2024 by the author. Licensee MDPI, Basel, Switzerland. This article is an open access article distributed under the terms and conditions of the Creative Commons Attribution (CC BY) license (https://creativecommons.org/licenses/by/4.0/).

1. Introduction

Coastal regions are heterogeneous areas with complex landscape patterns that reflect the interplay between natural ecosystems and human activities. The environmental settings of such areas reflect tight links between the terrestrial and marine natural ecosystems. On the other hand, coastal lands experience high anthropogenic pressure, such as intensive urban construction, industrial and agriculture activities, marine transport systems and harbours. Monitoring the dynamics of the shorelines is essential for effective land management, natural resource planning and urban development. Remote sensing (RS) data such as satellite images present a robust, reliable and cost-efficient information source to monitor coastal landscapes [1–3].

An important advantage of RS data is the long and ongoing tradition of their usage in environmental studies in general and for coastal regions in particular. This became possible due to the rich collection of RS data available through different satellite missions. As a result, a systematic and comprehensive observation of the Earth's surface made through the use of satellite images provides rich informational background for deep insights into

the environmental analysis of climate-related processes. For instance, time series of satellite images are useful for analysis and modelling of landscape dynamics. Comparison of such data enables researchers to reveal important ongoing trends in coastal processes of the marine ecosystems: for instance, to visualise flood extents [4], to highlight the intensity of hazards [5] or to evaluate potential risks [6].

RS data are widely used for monitoring coastal and marine environments. Examples of the use of RS data in environmental studies include, for instance, the analysis of coastal erosion [7], monitoring vegetation and landscape dynamics [8,9], detection of seagrass distribution [10], assessment of water pollution and eutrophication [11], visualization of urban sprawl in coastal areas [12], mapping land cover changes [13], evaluating water quality [14–16] and computing eutrophic sea level rise or shoreline extraction [17]. Among these examples, detecting land cover changes plays a special role for coastal monitoring. In fact, it enables researchers to evaluate environmental trends, detect dynamics and provide data for the prognosis of possible scenario developments. Besides forecasting, detecting changes is crucial for evaluating climate–environmental interactions, as changing environments affect human well-being and destroy social systems through worsening living conditions. With this in mind, coastal monitoring enables researchers to better understand the complexity of such processes, which is essential for environmental planning and policy making [18,19].

Many studies have been undertaken recently for environmental coastal monitoring using RS data and GIS [20]. The aim of these and similar works is to detect crisis areas where landscape changes take place in order to spot and to map the affected regions for decision-making. For instance, human-induced processes may include urbanisation of coastal areas [21], agriculture plantations [22], unsustainable tourism [23,24] or climate-related processes affecting ecosystems [25,26]. These processes lead to the disruption of natural ecosystems. They also may trigger changes in land cover types [27], increase landscape fragmentation [28], destroy the connectivity between individual patches and cause deforestation. In the end, such effects misbalance coastal ecosystems and modify their structure.

Technically, detecting changes can be performed using time series analyses of RS data. This is possible through comparison of multi-temporal RS data covering the same area with different time intervals [29–31]. Spatial analyses supported by multi-temporal RS data can be further used to monitor and operatively detect such regions that are visible in satellite images from space. Nevertheless, the question arises: How can we effectively processes RS data, and which methods present the most efficient and optimised solutions? The traditional tools for geographic information systems (GISs) have restricted capabilities and limitations in speed and accuracy for RS data processing, as reported in relevant work [32–34]. Therefore, similar to our proposed methodology, new technical approaches are constantly being developed (e.g., [35]).

Novel methods and approaches arise in the rapidly developing era of high-performance computing. These enable researchers to overcome the existing issues related to RS data processing and satellite image classification. For instance, these include the use of general-purpose programming languages in cartographic applications, such as Python or R, application of deep learning (DL) [36,37], scripting techniques [38,39] and artificial intelligence (AI) algorithms [40,41]. The integration of RS data and these new technologies provides effective approaches to RS data handling for accurate and rapid image processing [42,43]. Such powerful combination of Earth observation data and ML tools present a principally new cartographic approach for mapping marine and coastal environments that can be effectively used for operative monitoring of marine and coastal areas [44].

Discriminating complex and highly fragmented patches of coastal landscapes requires the use of advanced methods for RS data processing. As a response to these needs, we utilise AI algorithms that enable us to accurately recognise and classify even tiny differences in landscape patches and to detect the dynamics of vegetation types. Moreover, workflow repeatability is facilitated by using scripting techniques of Geographic Resources Analysis

Support System (GRASS) GIS and Generic Mapping Tools (GMT). Such a combined use of different software ensures the flexibility of the cartographic techniques through the use of GMT for gridded raster data handling using available techniques [45], QGIS for vector data visualization and scripts of GRASS GIS for AI and ML methods of image processing.

This study is organised into two logical parts. The first part gives insights into the environmental setting of the coast around Phillip Port Bay, southern Australia, while the second one focuses on describing and presenting the technical tools. Here, we describe the details of the methods of the AI algorithms that were used for satellite image processing and point to the differences that exist between them. The results obtained from image classification are commented on in relevant sections with the sequential discussion, closing remarks and recommendations for future works.

2. Study Area

The research is focused on the area around Melbourne—the second largest city on the Australian continent—and encompasses Port Phillip Bay. The exact zone of the study area is restricted between the coordinates from 143°01′33.38″ E to 143°08′03.62″ E longitude and from 38°32′14.93″ S to 36°24′10.94″ S latitude. This area is located in the southern part of the state of Victoria, Australia (Figure 1).

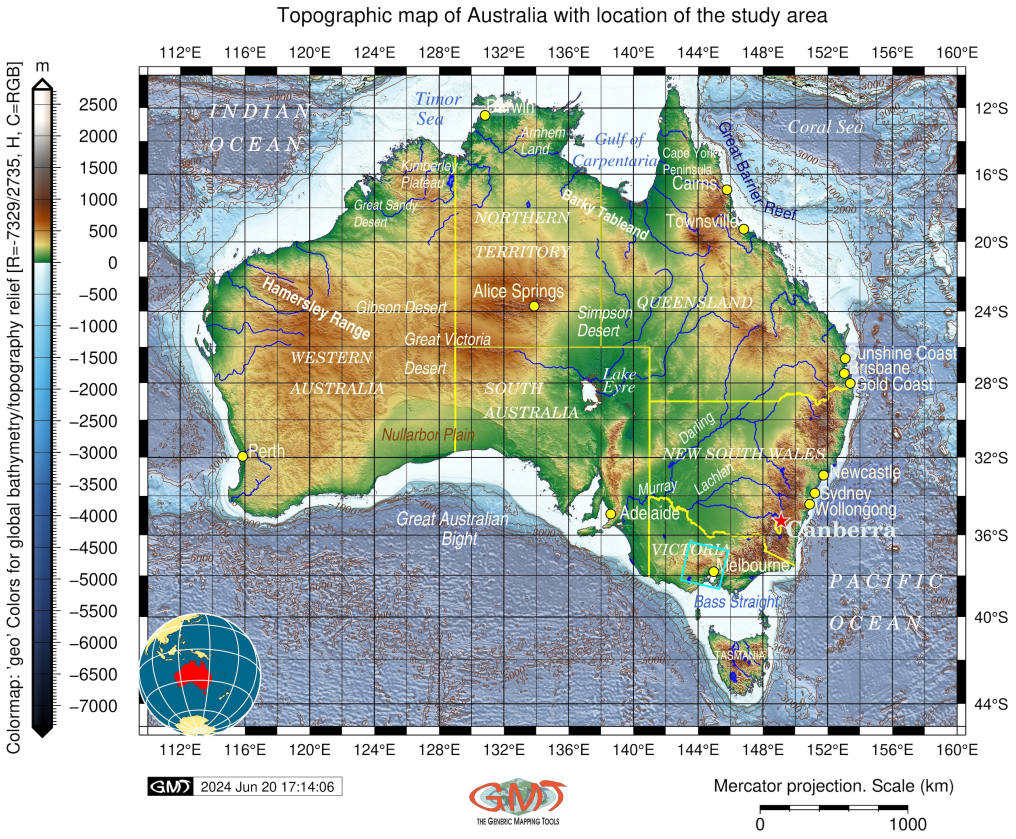


Figure 1. General topographic map of Australia with location of study area outlined. Mapping software: Generic Mapping Tools (GMT) version 6.4.0. Data source: GEBCO. Map source: author.

The state of Victoria comprises 79 municipalities. According to the 2023 census, Victoria has a population of 6,865,400 [46], which makes it the second-most-populated state (after New South Wales) in Australia. Such population density increases anthropogenic pressure on the natural environment of coastal areas. On the other hand, there is a strong link between the coastal environment and the quality of life for the population living in this area, which illustrates dense human–nature interactions [47,48]. One of the most prominent features in the environment of southern Victoria is the coastal plains of Port

Phillip Bay—the largest coastal lagoon system in Victoria, Australia (Figure 2). Port Phillip Bay presents an embayment formed between the end of the last ice age around 8000 BCE as a result of faulting and marine transgression. Nowadays, it is located in a shallow tectonic depression with depths mostly less than 8 m [49]. It has a total area of 1930 km^2 and forms a closed ecosystem with an irregular coastline, diversified topographic setting and complex geomorphology [50].

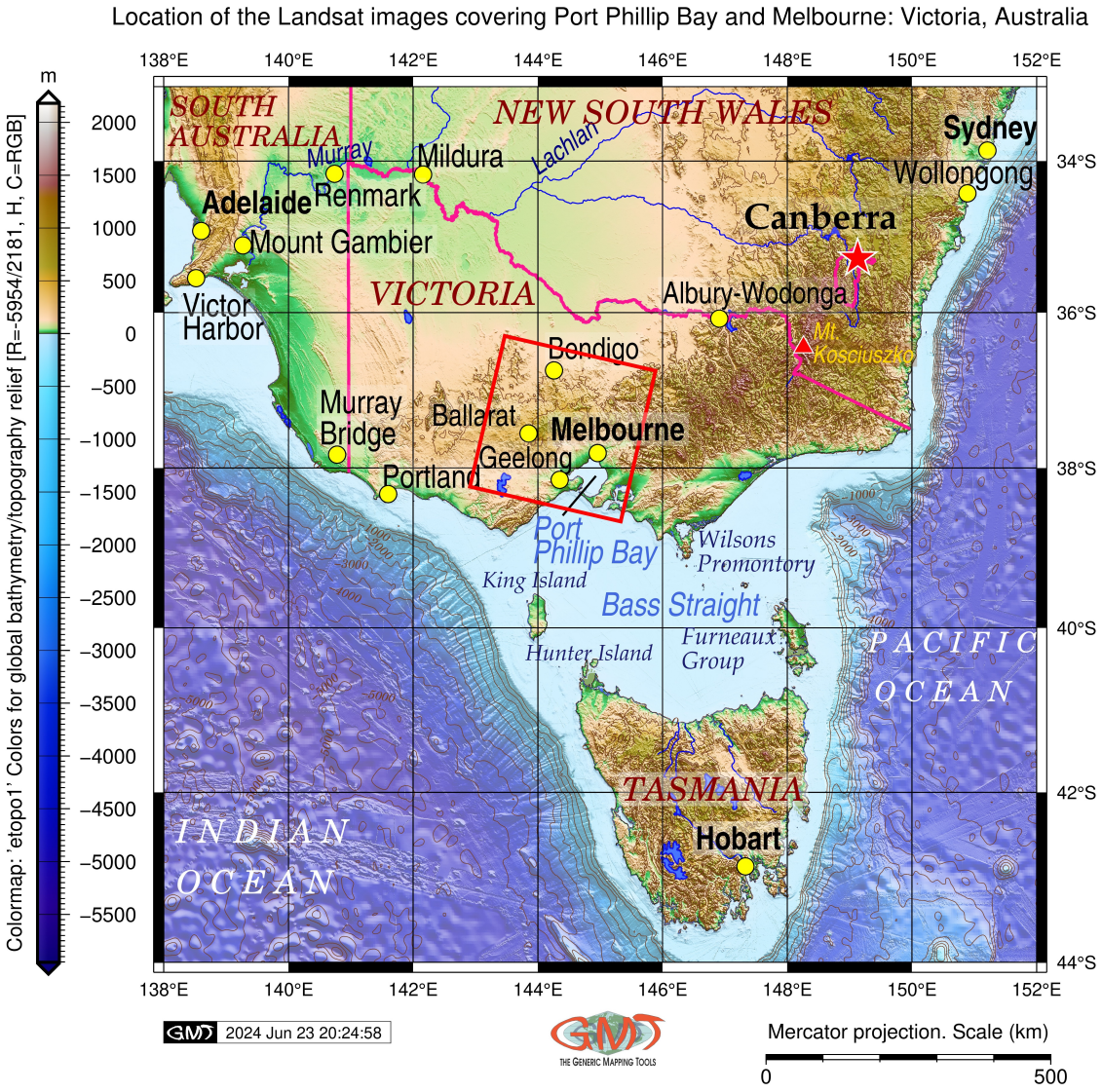


Figure 2. Enlarged fragment of a topographic map of southern Australia showing the location of the study area. Mapping software: Generic Mapping Tools (GMT) version 6.4.0. Hydrographic and topographic data source: GEBCO. Map source: author.

The dominating land cover types around Port Phillip Bay and southern Victoria include bushland, native shrubland, pastures and grasslands that intersperse with native forests (Figure 3). Arid zones located further from the coastal area are notable for drylands with sparse crops and rare treed vegetation coverage with scattered trees. Lacustrine and moderate dune systems are also found in the surroundings of Port Phillip Bay. The land affected by anthropogenic activities includes agricultural farmlands, areas occupied by horticulture and irrigated lands, lands used for recreation, as well as built up areas. Those are mostly presented as cities and urban settlements, including small towns and constructed artificial objects (roads, industrial facilities, etc.) (Figure 3).

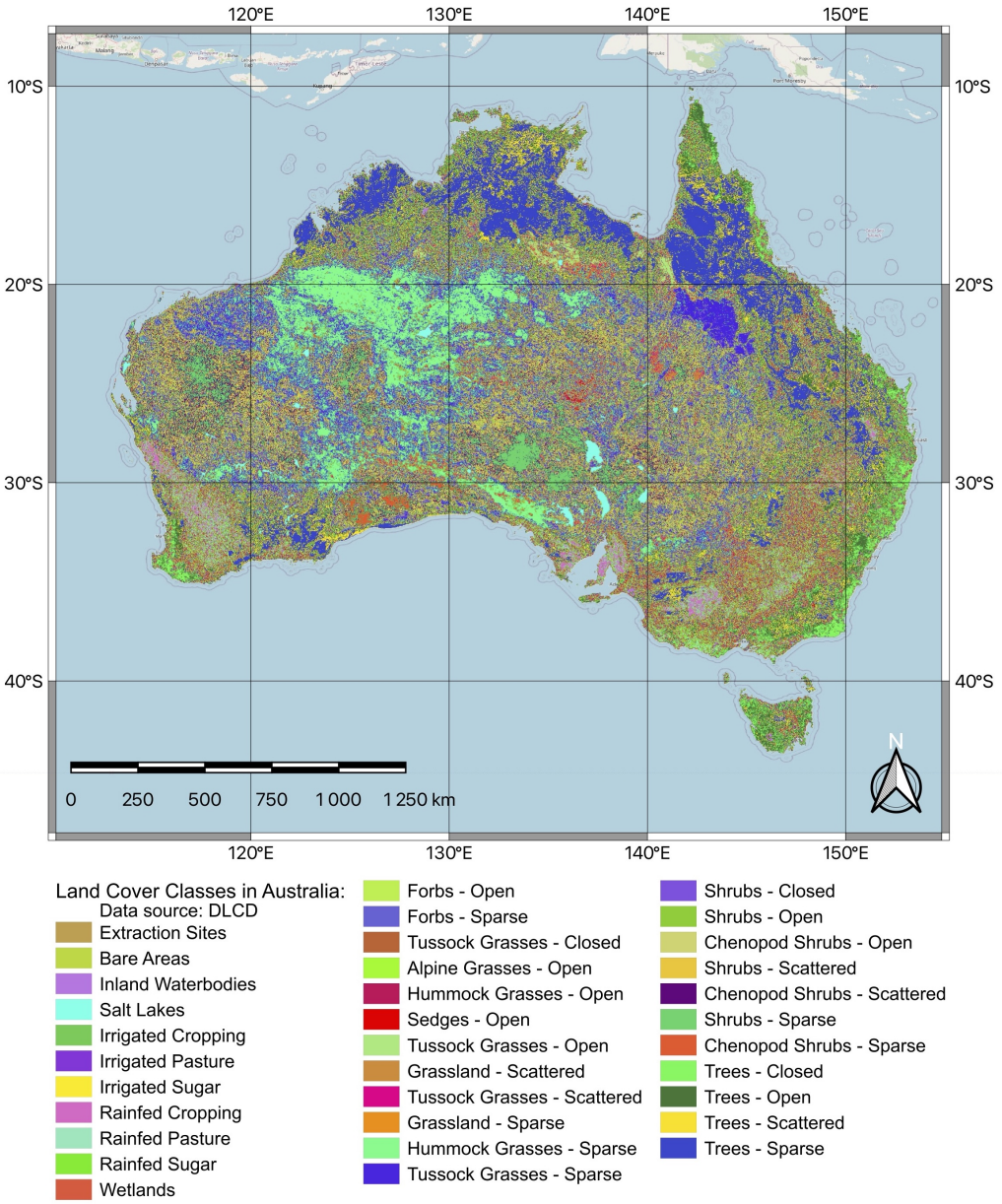


Figure 3. Land cover types in Australia. Mapping software: QGIS version 3.34.7 'Prizren'. Data source: Dynamic Land Cover Dataset (DLCD). Map source: author.

Landscape formation in this area is driven by diverse factors such as geologic foundations, climate and hydrological processes, e.g., wind forces, strong effects of oceanic waves, tides and currents. The variability of such processes affects nearby landscapes, controls the distribution of the land cover types and regulates general ecosystem functioning. As a result, the landscapes surrounding the estuaries of the Port Phillip Bay are presented as a complex mixture of types, including wetlands. Wetlands create a dynamic environment that supports rich marine and coastal biodiversity and important fisheries [51–53].

A recent environmental survey in the southern Victoria around Port Phillip Bay reported a distribution of 19,212 ha of coastal salt marshes, 5177 ha of mangroves and 3227 ha of estuarine wetland in this area [54]. Among these, the most notable system of wetlands is Cheetham, which occupies up to 420 ha of lagoons, including both artificial (salt marshes) and natural types (mangroves) (Figure 2). The high urbanization rate and constantly increasing population density of Port Phillip Bay is especially notable along the southern coasts of Victoria and within 100 km of coastlines. As a result, anthropogenic

pressure, exaggerated by industrial activities along the coasts, leads to the degradation of coastal areas and the deterioration of the landscapes around wetland areas [55]. Other environmental consequences include decreased water quality and excessive runoff of agricultural fertilizers, pesticides and chemical into Port Phillip Bay. Chemical pollution affects the water quality through high amounts of suspended sediment with nutrient inflows that cause eutrophication.

Cheetham Wetlands are distributed on old salt works land in the western part of Port Phillip Bay and include seasonal and perennial types that are protected for conservation purposes. Located ca. 20 km southwest of Melbourne [56], the perennial Cheetham Wetlands dry occasionally, but only during periods with low precipitation [57]. However, much of the flora and fauna are not adapted to drying and remain permanently in the areas filled with water. Such settings create a unique environmental ecosystem with specific species that are adapted to such conditions of variable water levels. The hydrological and climate setting of Cheetham Wetlands favour its high environmental value by providing a habitat to over 200 species of rare birds. Apart from regional species, they also include migratory birds that move to the Southern Hemisphere between July and November [58].

The current environment of Port Phillip Bay has developed due to a complex interaction of climate, lithological variability, tectonic–geologic deformation and sea level changes. Nowadays, regional land cover types continue changing further both along the coastline and in the hinterland. This is mainly caused by human activities such as economic development, residential construction, urban sprawl and recreational pressures [59]. Current environmental issues in this area include anthropogenic threats such as commercial dredging, water pollution and contamination caused by trace metals, toxic substances, organochlorines and hydrocarbons [60]. Recent studies also detected changes in the structure and composition of benthic communities as well as weed invasions in Port Phillip Bay caused by environmental interactions [61]. Finally, the shallow bathymetry of the bay contributes to eutrophication [59] and marine algae blooms [62,63] in selected parts of the embayment. As a result, the overall condition of Port Phillip Bay appears to have deteriorated on a large scale over recent decades [64].

3. Materials and Methods

An approach that integrates RS data and AI algorithms is proposed herein to identify land cover changes through pixel-level mapping for environmental monitoring of the southern area of Victoria (state), Melbourne district.

3.1. Data

The data used in this study for spatial analysis and image processing were obtained from open sources. The geospatial data of GEBCO (https://www.gebco.net/, accessed on 24 June 2024) with a 15 arc second spatial resolution was incorporated for topographic mapping. A general topographic map with the location of the study area within Australia outlined was plotted based on the General Bathymetric Chart of the Oceans (GEBCO) dataset with 15 arc minute resolution, as shown in Figures 1 and 2 generated using GMT. The GMT cartographic scripting toolset was developed by Paul Wessel and Walter Smith in Lamont-Doherty Earth Observatory, Palisades, New York, USA, and now supported by S. Wessel and volunteers worldwide under the GNU Lesser General Public License. The names of the major features, cities and geographic objects were obtained from the Gazetteer of Australia (Aggregator: Geoscience Australia, distributed under a Creative Commons Attribution 3.0 license).

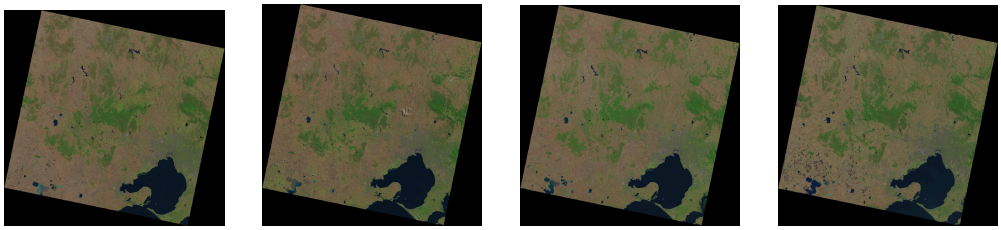
The land cover type reference data were obtained from the open repository of Geoscience Australia of the Australian Government. In this dataset, categories are identified based on updated classified imagery of Geoscience Australia Landsat land cover with resolution of 25 m that replaces the previous version based on classified images from the Terra Moderate-Resolution Imaging Spectroradiometer (MODIS). Nowadays, this dataset presents a nationally consistent and thematically comprehensive land cover

reference for Australia—the Dynamic Land Cover Dataset (DLCD), version 1.0.0 (https://knowledge.dea.ga.gov.au/data/product/dea-land-cover-landsat/?tab=overview, accessed on 24 June 2024) (Figure 3). These data were used to obtain the general characteristics of the landscape types in Port Phillip Bay and its surroundings. The vector layers of these data were processed and visualised using QGIS software version 3.38.1, name of the software developer company: QGIS Development Team; developed under License GNU GPLv2.

Coping with the diversity of information in RS data with different spatio–temporal or categorical attributes poses a prevalent difficulty in satellite image processing. With this in mind, selecting data with suitable spatio–temporal parameters plays a crucial role in mitigating this challenge by furnishing tailored suggestions. Thus, environmental analyses take advantage of diverse aspects of RS, such as the physical fundamentals of spectral reflectance and orbit characteristics that accommodate various satellite missions. To compare some of the different types of RS, a single Satellite Pour l'Observation de la Terre (SPOT) image covers a footprint of 3600 km^2 at resolutions of 20 m to 2.5 m, with a location accuracy up to 10 m; Landsat 8–9 OLI/TIRS imagery has a resolution of 30 m in multispectral bands; Sentinel-2 imagery has different resolutions in four bands at 10 m, six bands at 20 m and three bands at 60 m spatial resolution.

The spatial data variability and differences in their technical characteristics illustrated by the examples above require adjusted approaches, such as ML and AI, to handle these data in order to obtain geo-information effectively. Therefore, the RS data used in this study were obtained from the Landsat Operational Land Imager and Thermal Infrared Sensor (OLI-TIRS), United States Geological Survey (USGS). The data were selected due to their high quality, acceptable resolution, robust technical characteristics and cloudless coverage of the study area. The main metadata of the satellite images are summarised in Table 1.

Technically, the multispectral Landsat 8-9 OLI-TIRS images were retrieved from the Earth Explorer repository (https://earthexplorer.usgs.gov/, accessed on 24 June 2024). The metadata were acquired and checked for cloud coverage, image quality and image extent to cover the entire study area of Port Phillip Bay. Four satellite images were obtained for the following dates in the month of March: 26 March 2013, 29 March 2015, 18 March 2017 and 29 March 2024. These images from the raw dataset in natural colours are presented in Figure 4.



(**a**): March 2013 (**b**): March 2015 (**c**): March 2017 (**d**): March 2024

Figure 4. Original data: Landsat 8–9 OLI/TIRS images of Phillip Bay, southern Australia, collected during March during the years 2013, 2015, 2017 and 2024. Source: USGS. Compilation source: author.

Some major technical characteristics common to all Landsat scenes are as follows: the satellite images have an L2 data level type (meaning they incorporate geometric correction and topographic correction based on parameters from an OLI TIRS L2SP sensor identifier), the collection category is T1, the collection number is 2, and ground control points (GCP) are version 5. The spacial resolution is 30 m for multispectral channels and cirrus (bands 1 to 7 and band 9), 15 m for panchromatic (band 8) and 90 m for the thermal infrared sensor (TIRS) (bands 10 and 11). The cartographic parameters are the following: the data are projected in Universal Transverse Mercator (UTM), the zone is 55 South, the datum and ellipsoid are WGS84. The satellite ID is 9 for the scene in 2024 and 8 for the rest of the images, and the station identifier is LGN for all the data. All images were taken at the nadir in day time. The Worldwide Reference System (WRS) path is 93 and the row is 86.

Table 1. Metadata for the four scenes of the Landsat 8–9 OLI/TIRS images used for RS data processing and classification.

Dataset Attribute	Attribute Value: 2024	Attribute Value: 2017	Attribute Value: 2015	Attribute Value: 2013
Landsat Product Identifier L2	LC09_L2SP_093086_ 20240329_20240403_02_T1	LC08_L2SP_093086_ 20170318_20200904_02_T1	LC08_L2SP_093086_ 20150329_20200909_02_T1	LC08_L2SP_093086_ 20130326_20200913_02_T1
Landsat Product Identifier L1	LC09_L1TP_093086_ 20240329_20240329_02_T1	LC08_L1TP_093086_ 20170318_20200904_02_T1	LC08_L1TP_093086_ 20150329_20200909_02_T1	LC08_L1TP_093086_ 20130326_20200913_02_T1
Landsat Scene Identifier	LC90930862024089LGN00	LC80930862017077LGN00	LC80930862015088LGN01	LC80930862013085LGN02
Date Acquired	29 March 2024	18 March 2017	29 March 2015	26 March 2013
Roll Angle	0.001	0.000	0.000	0.000
Date Product Generated L2	3 April 2024	4 September 2020	9 September 2020	13 September 2020
Date Product Generated L1	29 March 2024	4 September 2020	9 September 2020	13 September 2020
Start Time	29 March 2024 00:09:22	18 March 2017 00:09:03.868153	29 March 2015 00:08:50.482423	26 March 2013 00:10:37.681759
Stop Time	29 March 2024 00:09:54	18 March 2017 00:09:35.63815	29 March 2015 00:09:22.252419	26 March 2013 00:11:07.47778
Land Cloud Cover	0.34	0.26	0.48	0.13
Scene Cloud Cover L1	0.33	0.24	0.45	0.12
Ground Control Points Model	1160	1194	1171	1081
Geometric RMSE Model	5.002	4.048	4.001	4.701
Geometric RMSE Model X	3.304	2.534	2.419	3.135
Geometric RMSE Model Y	3.756	3.156	3.188	3.503
Processing Software Version	LPGS_16.4.0	LPGS_15.3.1c	LPGS_15.3.1c	LPGS_15.3.1c
Sun Elevation L0RA	38.05564986	41.13467347	38.22640744	39.13419122
Sun Azimuth L0RA	45.77175870	50.09114471	46.16829406	46.70481697
TIRS SSM Model	N/A	FINAL	ACTUAL	ACTUAL
Scene Center Latitude	−37.47464	−37.47435	−37.47440	−37.47462
Scene Center Longitude	144.35289	144.40120	144.39626	144.31862
Corner Upper Left Latitude	−36.40217	−36.40099	−36.40088	−36.45905
Corner Upper Left Longitude	143.10763	143.15450	143.15116	143.11148
Corner Upper Right Latitude	−36.45824	−36.45609	−36.45602	−36.51418
Corner Upper Right Longitude	145.66861	145.71886	145.71217	145.59395
Corner Lower Left Latitude	−38.47670	−38.48103	−38.48092	−38.42299
Corner Lower Left Longitude	142.99849	143.04638	143.04295	143.00833
Corner Lower Right Latitude	−38.53712	−38.54041	−38.54033	−38.48215
Corner Lower Right Longitude	145.63117	145.68274	145.67586	145.55655

3.2. Workflow

The workflow steps to process and classify the satellite images in order to detect land cover types along the coastal landscapes of southern Australia are schematically presented in Figure 5.



Figure 5. Workflow methodology. Software: RStudio version 2024.04.2+764, R version 3.6.0, 'DiagrammeR' package version 1.0.11.9000. Diagram source: author.

Employing ML and AI techniques of GRASS GIS involves a multi-step process. The first stage involves data import through the modules 'r.import' or 'r.in.gdal'. The formulation of the initial data check includes metadata control using the 'r.info' and 'r.category'

modules, which provides information on the raster map layer and evaluates the values and labels of categories, respectively. Among other functions, this enables us to check the background information about the geographic extent of the study area and the variables in an analysis of the raster layer. The 'g.copy module' copies the existing raster maps in the mapset, which is controlled by the module 'g.list rast' for evaluating its current content.

During the second stage (image processing), GRASS GIS begins to explore the images by generating corrected scenes. To this end, atmospheric correction, geometric rectification and calibration are applied using the modules 'i.landsat.toar', 'i.rectify' and others. At this stage, the quality of the multispectral bands of Landsat is improved to facilitate the next steps of image classification by the AI and ML algorithms. Cartographic handling enables us to tune up the region extent, visualise the data, add an explanatory legend, create coloured composites from the multispectral triplets and select representative colours for each map using several modules: 'd.rast', 'd.legend' and 'r.colors'. In the next stage, GRASS GIS narrows the focus of image processing for the ML algorithms (RF, SVM, MLP, etc.) and evaluates the cell values using a computer vision approach. The pixels are automatically distributed and grouped into classes according to their DNs.

This process involves the use of modules 'r.random' and 'r.learn.train' and other algorithms, as presented in the schematic diagram (Figure 5). The ML part is performed using algorithms from the scikit-learn package of Python, which is integrated with GRASS GIS, version 8.3. In the final stage, the classification of the images is finalised with map outputs and an accuracy assessment. The latter includes computing the rejection probability accuracy using the chi-square algorithm, generating a statistical report, and computing class separability matrices for each year of the evaluated Landsat scenes. At this point, the quality of processed data is assessed using particular algorithms embedded into GRASS GIS.

The cluster parameters for the MaxLike classification approach were accepted with the following values. The number of initial classes is 10, the minimum class size is 17, the minimum class separation is zero, and the percent convergence is 98.0 for all the scenes. The maximum number of iterations is 30, as defined by the GRASS GIS algorithm. The statistical summary of the accepted computational parameters for image processing through clustering is given in Table 2.

Table 2. Statistical parameters for clustering using 'i.maxlik' module of GRASS GIS.

Year	Rows	Cols	Cells	Parameters of Clustering		
				Sample Size	Row Sampling Interval	Column Sampling Interval
2013	7281	7421	54,032,301	7044	72	74
2015	7711	7661	59,073,971	7005	77	76
2017	7711	7652	59,004,572	7011	77	76
2024	7692	7522	57,859,224	7217	76	75

The adjusted automatic classification model was performed using the 'i.maxlik' module of GRASS GIS, which employs the maximum-likelihood discriminant analysis classifier. The thematic map of land cover types was created using QGIS software to evaluate the distribution of major categories across the study area. Additionally, a digital elevation model (DEM) was obtained from GEBCO and was generated as a topographic map of study area to strengthen the environmental setting through geospatial information. Here, the initial values of the pixels were computed for each multispectral band of the Landsat scenes for each year (the results are reported in Appendix A). Then, an iterative process for the re-assignment of these pixels was performed (the results of the iteration cycles are reported in Appendix B for each year), and the pixels were harmonised and readjusted to the target classes through a repetitive sequence of the computational process.

Four widely used ML algorithms were applied to classify the images: (1) random forest (RF), (2) support vector machine (SVM), (3) an ANN-based approach using a multilayer perceptron (MLP) classifier, and (4) a decision tree classifier (DTC). The SVM is a non-parametric statistical learning classifier that was initially proposed by Vapnik [65] with

the aim of finding the optimal surface that divides each set of points into distinct classes according to their properties. The optimal surface here means a decision boundary that minimises the number of erroneously classified points. Such a logical approach increases the accuracy of the classification, which results in the high applicability of this method to image classification and explains its high accuracy.

The maps obtained based on the classified images were visualised using the sequence of modules 'd.rast', 'd.grid' and 'd.legend' (Figure 6). Such a workflow made it possible to automate the necessary procedures to carry out image analysis. Additional information from the spectral bands (one to seven) was obtained and was statistically processed to evaluate changes during the period from 2013 to 2024.

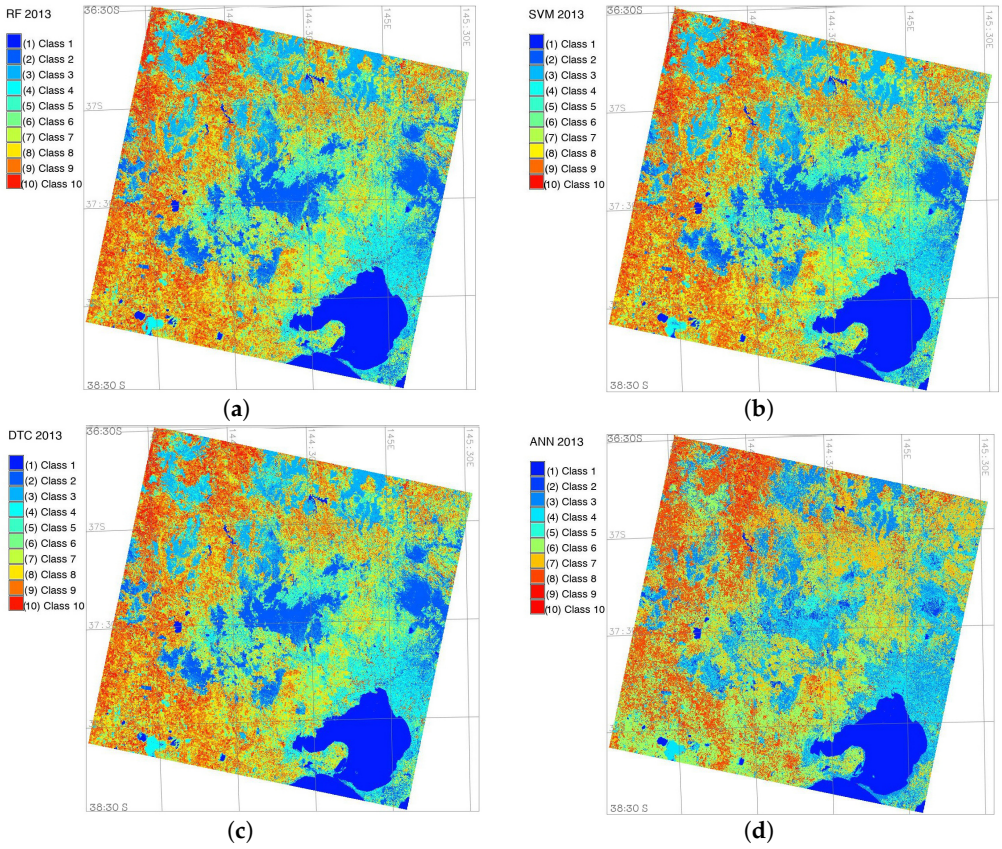


Figure 6. Results of image processing of images from 2013 using four methods: (**a**) random forest (RF); (**b**) SVM; (**c**) decision tree classifier; (**d**) ANN-based MLP classifier. Image processing: author.

Since all four ML and AI models that were applied belong to the type of supervised classifiers, a training dataset was necessary for their algorithms. A training dataset teaches the model to learn the patterns of the different classes that should be discriminated. To this end, a sample of unsupervised classification with pixel points was collected via clustering to train the ML and AI algorithms (Figure 7). This initial raster dataset was augmented through visual recognition of satellite images using the data on land cover types that were collected as reference from the Dynamic Land Cover Dataset (DLCD) open repository of the Australian government.

Four different ML and AI algorithms were tested, and their performances were evaluated. For SVM and RF, the optimal parameters of the models were adjusted to improve the classification performance and accuracy of assignment. At the same time, for all the years (2013–2024), the assignment of pixels to various land cover classes was evaluated for each band; this was calculated to understand the contribution of land cover types within the whole landscape in the classification models. The programming scripts and codes of GRASS GIS that were used for AI- and ML-based RS data processing and the reports on image

classification are available in the GitHub repository of the author for technical reference: https://github.com/paulinelemenkova/Australia_GRASS_GIS_AI_ML (accessed on 18 July 2024).

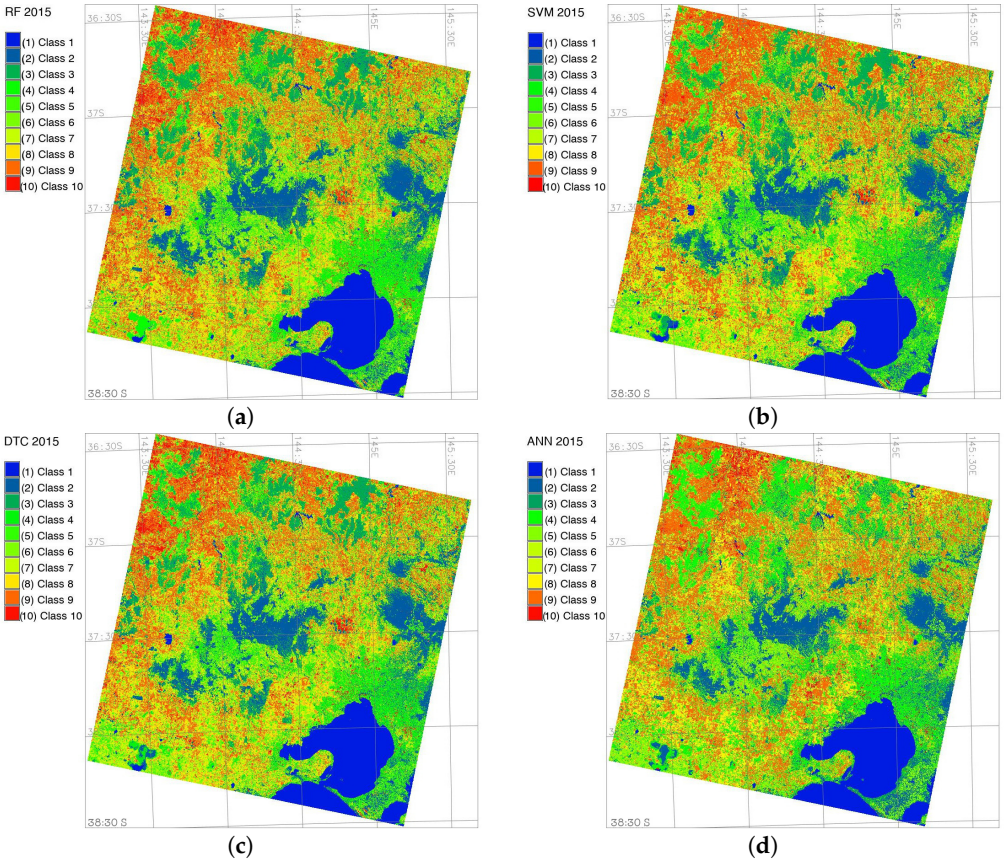


Figure 7. Image processing for images from 2015 using four methods: (**a**) RF; (**b**) SVM; (**c**) ANN-based MLPC; (**d**) DTC. Image source: author.

4. Results

4.1. Classification Output

The results of the classification of the satellite images using ML and AI methods are presented in Figures 6–9 for comparison of different approaches for years 2013, 2015, 2017 and 2024. Contrariwise, the time series of one algorithm but evaluating the environmental dynamics is illustrated in Figure 10. The computed statistics on land cover class distribution by multispectral bands for each Landsat image and by year for each evaluated period (2013, 2015, 2017 and 2024) were obtained and are summarised in the tables presented in the following section as well as in the Appendix B of this study, e.g., Table 3 for 2013 and likewise for the next periods. For 2013, pixels were assigned to the corresponding categories of the 10 recognised classes with 98.27% points of stable accuracy and convergence of 98.3% (Table 3).

Figures 7 and 8 display the results of the image classification approach using four different AI and ML methods by GRASS GIS, which resulted in ten land cover classes as described using seven multispectral bands from the 2015 and 2017 Landsat images. Visually, these maps reflect broad land use land cover (LULC) characteristics of Cheetham Wetlands, a section of the marsh and the uplands surrounding Port Phillip Bay. Cheetham Wetlands and marsh area (Class 7) are bounded to the west by upland vegetation including mixed tree cover, sparse vegetation and scattered trees (Class 5) as well as scrubs, bushland and shrubland (Class 2). The marsh areas and wetlands are partially mingled with other cover classes and inclusions of single trees and bushes that have adapted to the wet conditions.

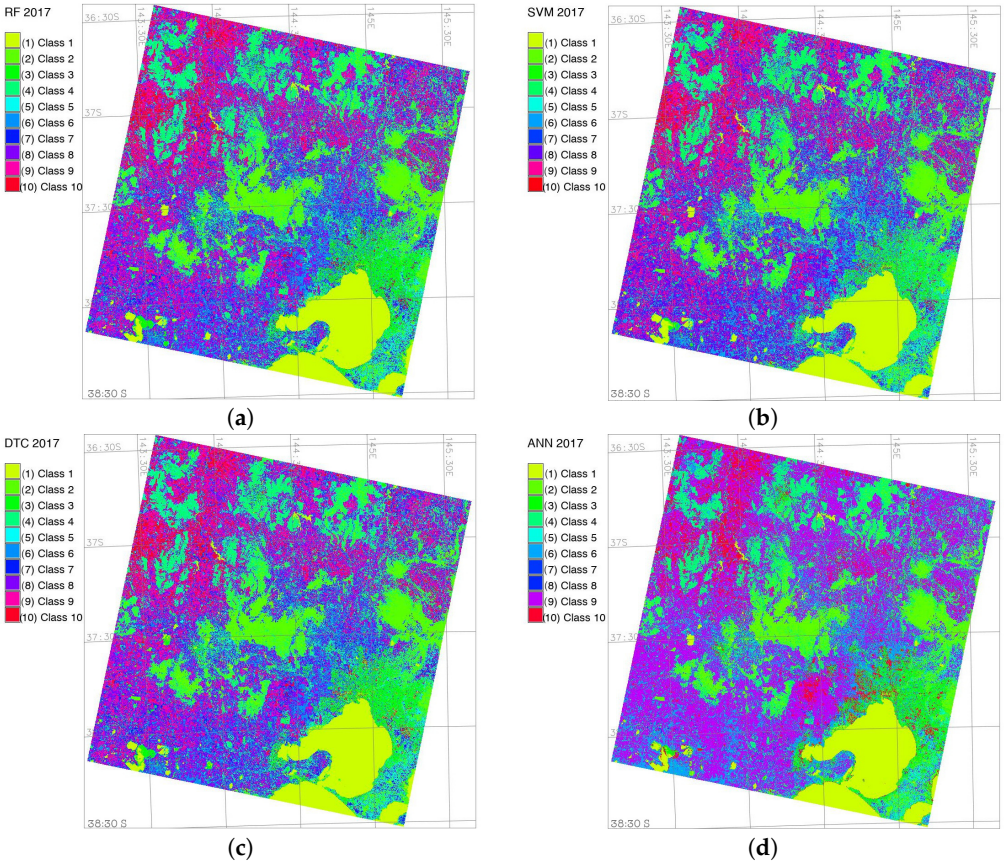
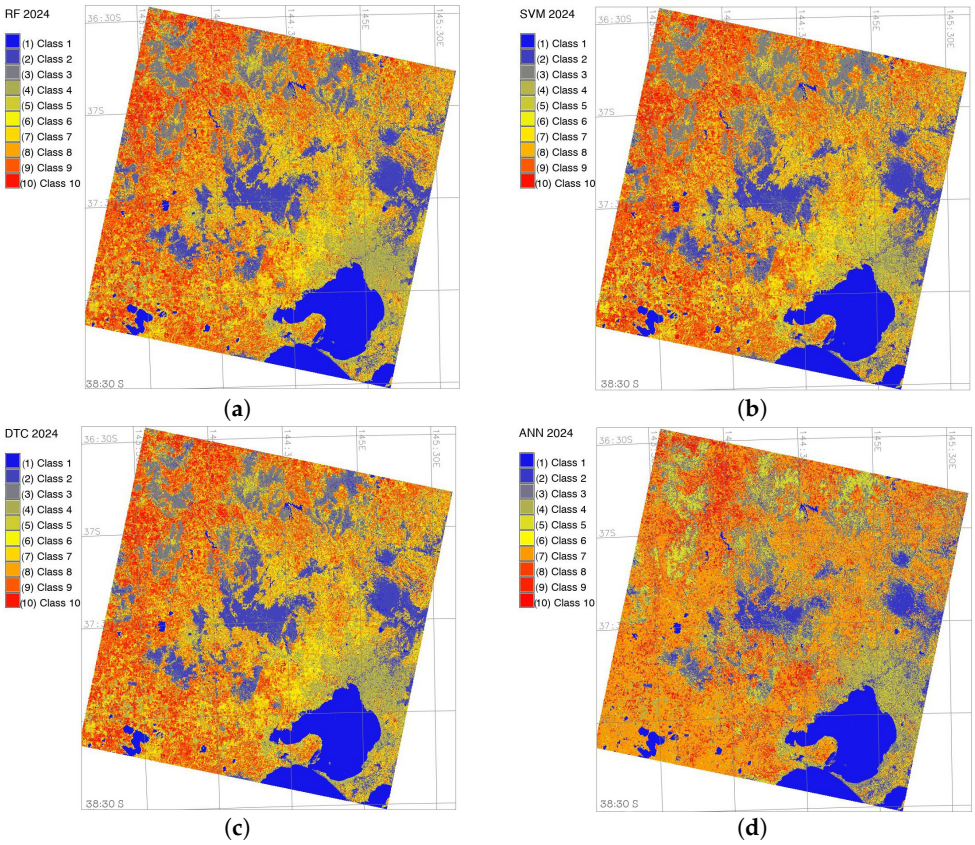


Figure 8. Results of image processing for images from 2017 using four different methods: (**a**) random forest; (**b**) support vector machine (SVM); (**c**) ANN-based approach using MLP classifier; (**d**) decision tree classifier. Image processing source: author.

The selection of the land categories was employed using data adopted from southern Australia and Port Phillip Bay. The adaptation of these data aimed at the correct detection of coastal landscapes within the ecosystems of southern Victoria, with the special aim of detecting wetlands and discriminating them automatically from urban areas and native forests. A retrospective time series for 1987–2019 over Victoria (state) was employed (https://www.environment.vic.gov.au/biodiversity, accessed on 25 July 2024): (1) water bodies (Port Phillip Bay, lakes and rivers), (2) bushland, (3) farmland and cropland used for agriculture, (4) native forests (closed trees), (5) sparse vegetation and scattered trees, (6) recreational land, (7) wetlands, (8) built-up areas, (9) pastures and grasslands, and (10) bare areas.

To the east along the Indian Ocean, developed land appears as a segment immediately adjacent to the open coastal spaces. This includes a section of marshes with beachfront development that is notable by real estate of compact beach front construction close to the water's border. The classes of natural vegetation are also observed in other segments of the classified scene and include features such as native forests (closed trees), sparse vegetation and scattered trees in drylands. The regions marked by anthropogenic activities (Class 8) include built-up areas, which comprise constructed commercial and residential buildings, roads and adjacent parking places and related objects of infrastructure. A distribution of farmland and cropland (Class 3) is notable in the eastern areas, where there are more intense agriculture activities.



(**a**) (**b**) (**c**) (**d**)

Figure 9. Image classification for images from 2024 using four methods: (**a**) random forest; (**b**) SVM; (**c**) ANN-based MLPC; (**d**) DT classifier. Image processing: author.

Table 3. Pixelwise computational statistics on land cover class distribution by spectral bands from imagery from 2013.

Class	Multispectral Bands of the Landsat 8 OLI/TIRS Scene for 2013							
	Stat	B1	B2	B3	B4	B5	B6	B7
1 (507)	means	7687.78	7908.5	8088.38	7475.44	7336.59	7412.26	7391.69
	stdev	344.653	421.512	668.419	537.547	460.436	295.948	180.949
2 (638)	means	7680.67	7842.55	8326.59	8342.63	14,223.1	10,929.8	9067.1
	stdev	222.242	267.302	375.086	444.833	1553.37	856.04	567.558
3 (887)	means	8097.13	8335.14	8934.32	9236.08	14,634.2	13,461.6	10,833.1
	stdev	256.84	273.675	349.578	379.762	1150.47	761.219	550.821
4 (617)	means	8656.62	9001.7	9802.38	10,300	14,321.4	14,803.1	12,391.7
	stdev	610.8	666.747	803.156	815.317	969.65	962.333	703.455
5 (378)	means	8457.53	8775.73	9744.8	10,004.9	17,329.6	16,009.9	12,429.8
	stdev	635.538	594.932	704.354	866.12	1584.96	1076.47	793.116
6 (748)	means	8753.46	9158.45	10,033.5	10,785.5	14,633.9	17,307.8	13,990.3
	stdev	306.286	344.408	426.607	563.988	788.463	802.195	664.108
7 (584)	means	8868.88	9316.54	10,365.6	11,059.3	16,695	18,546	14,492.1
	stdev	240.485	270.356	368.04	570.249	1012.67	773.668	561.7
8 (1004)	means	9161.49	9674.29	10,660.8	11,716.9	15,122.4	19,256.5	15,629.3
	stdev	354.297	391.741	494.712	625.917	665.09	805.656	665.977
9 (1175)	means	9392.39	9999.52	11,149.5	12,418.8	16,298.3	20,847.9	16,690.6
	stdev	251.846	295.699	411.786	635.913	797.684	750.01	752.185
10 (506)	means	9967.75	10,719.8	12,141.4	13,725.9	17,504.8	22,182.4	18,140.5
	stdev	919.948	1000.56	1198.41	1274.36	1105.95	1361.48	1327.76

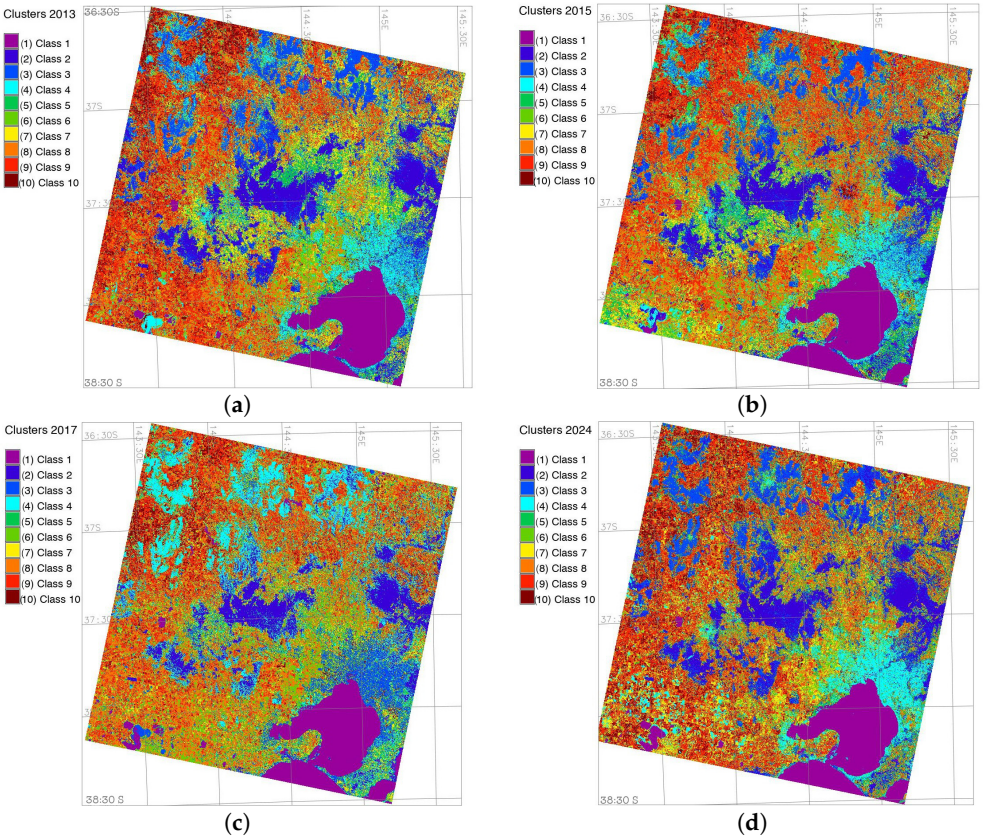


Figure 10. Time series of the classified images (2013–2024) processed using k-means clustering. (**a**) image on 2013; (**b**) image on 2015; (**c**) image on 2017; (**d**) image on 2024. Image processing: author.

The shallow water in Port Phillip Bay is distinct in colour from the waters of the Indian and Pacific Oceans; it is typified by very low lying areas near river and creek edges, and it is also marked by existing pools, wet soils along the coasts and low marsh vegetation along creek edges that belong to the hydrological system of Cheetham Wetlands. Likewise, the class of coastal marshes and wetlands also contains a few smaller pools and marginally wet areas where specific types of vegetation develop.

4.2. Statistical Metrics

Table 4 shows the evaluated statistical metrics derived from the computations obtained for each multispectral class for images from 2015.

Likewise, the performances for image classification for years 2017 and 2024 are summarised in Tables 5 and 6. They show the variations in pixels' means and standard deviations for pixels from the Landsat channel.

The overall trend in land cover type distributions by classes and the dynamics of changes is presented in Table 7. Here, the statistical results of the class distribution of the assigned pixels are based on the evaluated signature file for four years and seven multispectral bands, as summarised in Table 7, which shows target land cover types for 2013–2024. Land cover class 1 (water—Port Phillip Bay, lakes and rivers) demonstrated fluctuations, with a slight increase in 2015 and 2024, which points to climate effects and higher precipitation.

The borders of marshes and wetlands include an edge or the transitional intertidal zone between the main area of Cheetham Wetlands and the transitional zone that includes scrubs, shrubland and bushland as well as a mixed single tree cover zone. In contrast to the wetlands, the areas of farmland and cropland used for agriculture are mostly distributed at higher elevations and are surrounded by the wetlands and marshes in the coastal areas; the farmland and cropland are less prone to inundation due to their topographically elevated

areas and drainage channels. Forest communities and woody vegetation are predominantly distributed in higher elevated areas further from the beachfront area. The bushland, scrubs and shrubland class includes patches of mixed woody vegetation within wetlands and along their edges.

Table 4. Pixelwise computational statistics on land cover class distribution by spectral bands of Landsat-8 OLI/TIRS images from 2015.

Class	Stat	Multispectral Bands of the Landsat 8 OLI/TIRS Scene for 2015						
		B1	B2	B3	B4	B5	B6	B7
1 (568)	means	7940.28	8075.57	8123.99	7524.04	7425.85	7399.9	7372.91
	stdev	344.325	379.953	593.974	522.724	652.721	335.877	246.953
2 (615)	means	7686.57	7824.36	8272.39	8270.83	13,898.8	10,527	8863.34
	stdev	305.668	359.903	482.018	521.82	1537.46	845.958	552.008
3 (781)	means	8072.26	8269.64	8837.17	9086.89	14,572.4	13,012	10,576.3
	stdev	259.275	259.011	320.839	364.833	1119.29	746.203	547.4
4 (703)	means	8650.11	8941.9	9661.26	10,136	14,137.3	14,558.4	12,268.6
	stdev	617.366	675.844	814.999	863.171	1032.01	978.397	738.674
5 (391)	means	8462.31	8728.8	9605.56	9842.91	17,552	15,561.5	12,141.8
	stdev	293.506	297.3	383.437	489.254	1738.29	1098.23	795.876
6 (796)	means	8861.33	9180.17	9941.97	10,635.8	14,647.6	17,004.9	13,981.4
	stdev	356.821	369.241	445.523	545.923	900.559	805.354	717.999
7 (582)	means	8969.33	9327.61	10,291.4	10,917.5	17,000.9	18,508.4	14,546.8
	stdev	476.562	385.029	458.457	582.109	1075.41	907.064	678.588
8 (1026)	means	9211.47	9575.03	10,376.8	11,287.4	14,865.5	19,153.9	15,775.7
	stdev	278.492	282.228	361.572	493.88	732.319	843.458	637.941
9 (1245)	means	9452.33	9909.68	10,884.4	11,989	15,914.4	21,031.7	17,155.4
	stdev	237.238	250.904	380.325	578.133	859.887	805.656	762.815
10 (298)	means	10,110.3	10,774.9	12,172.6	13,679.5	17,597.3	22,695	19,191.3
	stdev	1645.09	1738.58	1908.73	1940.05	2142.28	1510.8	1592.87

Table 5. Pixelwise computational statistics on land cover class distribution by spectral bands of Landsat-8 OLI/TIRS images from 2017.

Class	Stat	Multispectral Bands of the Landsat 8 OLI/TIRS Scene for 2017						
		B1	B2	B3	B4	B5	B6	B7
1 (581)	means	7929.46	8108.94	8337.41	7709.38	7490.57	7424.3	7396.55
	stdev	337.158	410.139	735.841	802.125	750.097	360.916	220.256
2 (673)	means	7679.48	7836.62	8328.88	8317.19	14,848.9	10,861.6	8990.81
	stdev	223.056	254.243	345.482	464.513	1369.21	883.749	560.842
3 (494)	means	8537.22	8839.63	9573.69	9971.95	13,978	13,613.1	11,552
	stdev	633.576	671.098	776.416	867.675	1093.82	1071.02	823.154
4 (674)	means	7962.61	8209.86	8883.57	9075.13	16,186	13,121.2	10,398.7
	stdev	199.388	190.559	260.072	330.17	1246.94	716.604	522.388
5 (534)	means	8467.7	8822.3	9723.03	10,205.7	16,661.4	15,621.8	12,327
	stdev	459.728	463.622	524.131	604.138	1231.37	854.132	622.67
6 (836)	means	8762.76	9155.02	10,011	10,828.8	14,450.9	16,939	13,601.9
	stdev	394.902	369.181	436.331	516.127	772.106	926.651	639.347
7 (629)	means	8936.39	9422.97	10,520.8	11,467.8	16,778.1	18,160	14,163.3
	stdev	427.325	472.756	601.364	721.644	1091.77	848.855	622.946
8 (1048)	means	9073.67	9536.34	10,454.4	11,506.1	14,986.6	19,085.9	15,192
	stdev	296.637	272.932	327.833	442.594	650.591	671.502	648.356
9 (1140)	means	9304.19	9868.66	10,979	12,268.8	16,090.7	20,574	16,274.2
	stdev	265.901	270.652	382.621	538.007	823.946	719.359	763.055
10 (402)	means	9791.8	10,539.3	11,993.9	13,700.7	17,737.7	22,096.9	17,582.3
	stdev	893.661	985.953	1150.61	1206.94	1113.19	1082.1	1240.95

Table 6. Pixelwise computational statistics on land cover class distribution by spectral bands of Landsat-8 OLI/TIRS images from 2024.

Class	Multispectral Bands of the Landsat 8 OLI/TIRS Scene for 2024							
	Stat	B1	B2	B3	B4	B5	B6	B7
1 (609)	means	7766.02	8030.69	8320.34	7662.62	7371.63	7425.37	7425.87
	stdev	305.671	419.913	771.52	762.096	630.351	448.005	429.988
2 (670)	means	7624.08	7809.15	8313.88	8331.51	14,445.3	10,705.7	8901.21
	stdev	205.902	224.873	282.263	358.421	1258.89	839.254	538.858
3 (902)	means	7957.84	8235.82	8901.62	9185.04	15,515.2	12,986	10,380.8
	stdev	246.116	232.907	266.852	339.025	1083.85	732.316	535.359
4 (411)	means	8727.71	9082	9805.31	10,220.4	13,215.6	13,490.9	12,152.5
	stdev	668.955	673.146	789.834	850.916	1438.95	1133.67	998.25
5 (456)	means	8414.58	8770.55	9670.05	10,165.1	17,197.8	15,038	11,860.2
	stdev	558.686	585.325	697.741	839.222	1532.3	935.39	711.043
6 (712)	means	8683.41	9095.66	10,010	10,836.8	15,706	16,695.9	13,367.1
	stdev	367.576	376.232	457.499	563.708	983.967	895.602	565.674
7 (770)	means	9133.68	9581.99	10,492.9	11,575.9	15,226.5	18,332.2	15,088
	stdev	475.702	537.058	632.442	661.257	750.045	1015.51	778.522
8 (860)	means	9015.93	9521.11	10,624.3	11,889.1	17,408.1	19,159.2	14,827.3
	stdev	303.977	345.786	442.905	672.086	995.622	796.296	650.634
9 (1204)	means	9377.85	9895.28	10,950.8	12,359.9	16,667.9	20,878.6	16,604.8
	stdev	295.187	317.27	410.42	550.489	833.241	809.952	709.571
10 (623)	means	9883.75	10,559.2	11,938.5	13,760.8	18,445.9	22,327.5	17,691.4
	stdev	907.155	976.955	1174.7	1143.97	1143.34	1289.88	1481.44

Table 7. Class distributions of the assigned target pixels' land cover types for 2013–2024 during the iterative classification process.

Year	Classes of Land Cover Types									
	1	2	3	4	5	6	7	8	9	10
2013	1183	425	482	493	446	588	744	773	752	1158
2015	1215	367	471	491	485	589	731	782	774	1100
2017	1146	415	496	414	464	634	738	887	812	1005
2024	1249	514	541	434	440	522	671	784	806	1256

Ongoing climate–environmental processes and anthropogenic activities resulted in a slight decrease in land cover classes 5 to 7, which experienced changes to the occupied surface due to cumulative effects from aridification and human pressure along the coasts of southern Australia. Land cover class 8 (built-up areas) showed an increase over the recent decade, which indicates expansion of areas with impervious structures (e.g., such as roads, industrial construction and similar occupied lands). In contrast, the increase in pasture and grasslands (class 10) and bare areas (class 11) is notable for the recent decade, which might lead to soil degradation and initiate the deforestation of lands located in semi-arid environments (Table 7).

4.3. Interpretation of Trends

The effectiveness of different algorithms in supervised classification is based on the comparison of the information-filtering and information-extracting tools intended to anticipate and provide relevant content regarding LULC data obtained from the processed satellite imagery. Hence, a stable increase in land cover class 2 (bushland) is notable from 425 pixels in 2013 to 514 pixels in 2024, which signifies a decrease in forests in favour of minor plant types. The increase in land cover class 3 (farmland and cropland used for agriculture) by 2024 implies the intensification of irrigated lands used for commercial purposes. The distribution of forests (land cover class 4) demonstrates a slight decrease during the past decade from 493 pixels in 2013 to 434 pixels by 2024, which indicates slight

deforestation in the coastal areas of Port Phillip Bay, Victoria. The variations in land cover class 5 (sparse vegetation and scattered trees) indicate the initiation of the processes of restoration, which is the beginning of remediation for previously abandoned land.

The coastal part of Port Phillip Bay includes different natural habitats such as sandy beaches, rocky intertidal reefs, wetlands, mud flats, mangroves and salt marshes. Within the bay, habitats include seagrasses, rocky areas and bare marine sediments such as sands and silt. The results of land cover distribution in terms of artificial and natural land cover types correspond to recent classifications reported by the Port Phillip and Western Port Regional Catchment Strategy [66], which estimates that the urban area of Port Phillip Bay currently covers around 14% of the region, including infrastructure, bare spaces and associated areas; 44% of the region is used for cropland and agriculture, while 42% is classified as native vegetation on private land or on public land in reserves, parks and water supply catchments.

4.4. Comparison of Approaches

The ML algorithms that enabled us to extract such information using GRASS GIS scripting methods leverage methodologies to examine satellite images based on spectral reflectance, thresholds between categories for the assignment of pixels and raster cell attributes to produce maps. Here, the SVM, RF, MLPC and DTC algorithms demonstrated effectiveness in RS data processing. Using these tools, the RS data were categorised into content-based regional patterns of land cover types of southern Australia. To execute this ML classification using GRASS GIS, image preprocessing procedures were carried out (atmospheric correction, normalisation and cloud filtration), land cover features were extracted, the pixels were grouped into categories, the dataset was prepared, and four ML algorithms (RF, SVM, ANN-based MLPC and DTC) were trained.

The performance of the algorithms was evaluated to estimate the strength of the models used for satellite image classification. Among these, SVM and RF were predominantly effective due to the functionality of the algorithms, which increased accuracy results. Thus, the SVM model's performance demonstrated the best results, following by RF, which is caused due to the technical parameters of these algorithms. The advantages and high-performance of the SVM algorithm for image processing are explained by its theoretical approach: it locates a hyperplane of pixels that separates the maximum possible segment of raster cells on the image from the identical class on the same side while minimizing the distance between two or more classes. Such an approach is effective for the identification of land cover categories and pattern classification using Landsat data. Moreover, this algorithm keeps the distance between two or more classes as small as possible through effective separation of the data. This is based on the kernel function embedded in the algorithm, which provides the best separation of individual pixels on each multispectral band.

RF is one of the ML models that employs an ensemble method and a decision tree for the individual training data. Such an approach includes diverse models to make general predictions. Hence, it considers the variance between different models in order to give results that are more robust, less biased and have less variance. RF uses a bagging method, whereby raster pixels on the image are used to train the model. In this way, RF is not influenced by correlated variables, in contrast to DTC and other ML methods, because it uses a random selection of variables presented by cells to build trees. Therefore, after SVM, RF was demonstrated to be an effective image classification method with high performance for mapping coastal areas.

Furthermore, distinct and accurate (over 98% accuracy) performance was noted by the AI algorithm using MLPC. These methods incorporated additional information on the distribution of land cover types over southern Australia, i.e., landscape dynamics and trends over the recent decade. The overall accuracy of the SVM classifier was 97.6%, followed by 96.4% for RF. DTC showed lower results yet is comparable to the tested methods, with an overall achieved accuracy of 96.1%. Once the optical ML AI classifiers were determined for image processing, the time series analysis was plotted (Figure 10) to

visualise the dynamics of the land cover types in southern Australia between 2013 to 2024 along the coastal areas of Victoria. The decrease in areas occupied by Cheetham Wetlands around Port Phillip Bay was assessed over the recent decade using RS data processing and statistical analysis.

4.5. Accuracy Assessment

The accuracy assessment was computed using a chi-square algorithm, which evaluates the probability of the pixel's assignment to the correct class; the results are shown in Figure 11. The accuracy assessment was performed using the computed reject raster map, which presents the threshold. The threshold in these tables evaluates the limits according to which the pixels are assigned to the target classes correctly. It is possible to perform a chi-square test for each discriminant result at the tested threshold levels of confidence.

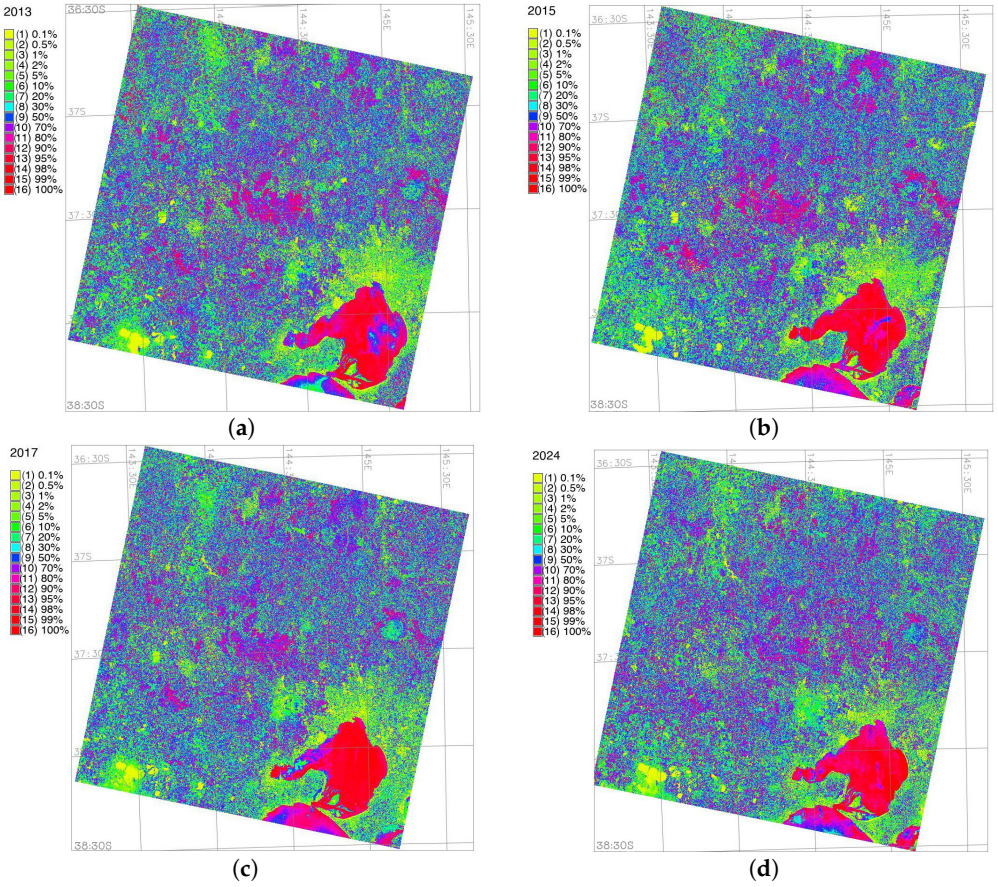


Figure 11. Accuracy analysis of image classification (2013–2024) using chi-square algorithm method. (**a**) image on 2013; (**b**) image on 2015; (**c**) image on 2017; (**d**) image on 2024. Image processing: author.

This test determines at what confidence level each pixel is classified to the correct category of land cover class. Hence, the reject threshold layer contains the index of the confidence level computed for each classified cell in the classified Landsat scene. The results of accuracy assessments evaluate the results observed during image processing. Additionally, the confusion matrices of the separability classes were computed to evaluate the correctness of the pixel's classification on the images for all the years: 2013 and 2015 (Figure 12) and 2017 and 2024 (Figure 13). These figures report the class separability matrices for land cover classes, which points to the accuracy from this classification with the four Landsat bands. The table in Appendix A shows the initial means for each band, and the table in Appendix B reports the iterative cycles of image classification for each Landsat scene.

	1	2	3	4	5	6	7	8	9	10
1	0									
2	2.2	0								
3	3.8	1.2	0							
4	4.1	1.8	0.9	0						
5	4.1	1.8	1.0	0.6	0					
6	6.0	2.9	1.9	0.8	0.8	0				
7	7.0	3.5	2.5	1.3	1.0	0.6	0			
8	7.3	3.8	2.8	1.6	1.4	0.9	0.7	0		
9	8.3	4.7	3.7	2.2	2.0	1.7	1.3	0.7	0	
10	6.0	3.7	3.0	2.1	1.9	1.8	1.5	1.2	0.7	0

	1	2	3	4	5	6	7	8	9	10
1	0									
2	1.8	0								
3	3.4	1.1	0							
4	3.6	1.7	0.9	0						
5	3.9	2.0	1.1	0.6	0					
6	5.3	2.8	1.9	0.8	0.9	0				
7	5.8	3.2	2.4	1.3	1.2	0.7	0			
8	6.8	3.9	3.1	1.6	1.8	0.9	0.7	0		
9	7.7	4.6	3.9	2.3	2.4	1.7	1.2	0.8	0	
10	4.8	3.3	2.9	2.0	2.1	1.7	1.3	1.2	0.7	0

Figure 12. Class separability matrices for land cover classes: 2013 and 2015.

	1	2	3	4	5	6	7	8	9	10
1	0									
2	2.1	0								
3	3.0	1.4	0							
4	3.4	1.1	0.9	0						
5	4.3	2.1	0.7	1.3	0					
6	5.2	2.8	1.0	2.1	0.8	0				
7	5.7	3.2	1.4	2.5	1.0	0.7	0			
8	7.2	4.0	1.8	3.4	1.6	0.9	0.6	0		
9	7.6	4.6	2.3	4.0	2.2	1.6	1.0	0.8	0	
10	6.1	3.9	2.4	3.4	2.2	1.9	1.4	1.4	0.8	0

	1	2	3	4	5	6	7	8	9	10
1	0									
2	2.0	0								
3	3.2	1.2	0							
4	2.6	1.6	1.0	0						
5	3.5	1.9	1.0	0.7	0					
6	4.6	2.9	1.9	0.9	0.7	0				
7	5.1	3.4	2.5	1.3	1.4	0.8	0			
8	5.8	4.0	3.0	1.6	1.5	1.0	0.6	0		
9	6.7	4.9	3.9	2.2	2.2	1.8	0.9	0.8	0	
10	5.3	3.9	3.2	2.2	2.1	1.8	1.3	1.1	0.7	0

Figure 13. Class separability matrices for land cover classes: 2017 and 2024.

The comparison of the data provides support for the overall classification procedure by GRASS GIS in that the land cover classes are spectrally separable on the multispectral Landsat scenes and that the AI and ML algorithms have worked quite well in these instances. The overall classification accuracy for the stratified random subset of points in 2013 was reported at 98.3% convergency with a Kappa coefficient of 98.27% points stable; for 2015—98.3% convergency and 98.34% points stable; for 2017—convergence = 98.1% and 98.12% points stable; finally, for 2024, we obtained 98.41% points stable with convergence=98.4%. Such results with the obtained Kappa coefficients above 0.80 mean that the overall classification accuracy by AI /ML algorithms of GRASS GIS approach is high.

5. Discussion and Conclusions

This study examined four AI applications of GRASS GIS for obtaining information on land cover changes in the coastal waters of Port Phillip Bay using data on spectral reflectance from multi-temporal Landsat satellite data (2013–2024). The spatial extent of these changes was visualised over the study area in the surroundings of southern Victoria (state), Australia. The presented maps are applicable for identifying hotspots for water eutrophication in the port, to detect the decline of native forest ecosystems and their replacement by urban spaces and to detect landscape dynamics on a regional scale relating to environmental–climate effects and anthropogenic activities.

The results of image classification using four different algorithms of AI and ML were compared to identify their effectiveness in GRASS GIS software, and the classification algorithms of ML and AI performed well in the case of both wetland cover classes and other categories. This approach enabled us to detect the areas experiencing the most intensive land cover changes in Port Phillip Bay, southern Victoria. Pixel-level mapping enhanced the identification of regions that required special focus; our flexible methodology increased the efficiency of the investigation by focusing on these specific areas, such as Cheetham Wetlands, which are distributed over the southern segment of the study area. A multi-disciplinary approach that integrated ML and RS data with GIS, as demonstrated in this study, ensures more insightful analysis of the interrelated processes along the coasts of southern Australia. As discussed earlier, the vulnerable coastal area along Port Phillip Bay is affected both by climate–environmental factors and by anthropogenic activities. This results in a highly dynamic and changing environment, which was detected over the time series of the satellite images.

Maps play a crucial role in environmental monitoring through visual analyses, which support environmental policy and management. Maps created using RS data within the framework of coastal environmental monitoring support decision-making through the

analysis of geospatial information. To support the decision-making process, the essential advantage of cartographic data visualization consists of spatio–temporal aspect of RS data and operative monitoring using time series. Using this information, we can always answer questions such as 'What changed in the landscapes ?', 'Where do these changes take place ?' and 'What is the level of changes (small to high) ?' Hence, the processing of satellite images primarily supports such decision-making processes and geospatial analysis through providing a visualisation of the extent of the affected areas and by mapping the exact locations of land cover changes. The targeted coastal areas that are affected either by environmental–climate processes or by human activities can be highlighted to find ways to mitigate the environmental crisis.

Earth observation datasets support such tasks in environmental monitoring. This becomes possible due to the significant development of satellite missions and techniques, which results in an increased quantity and variety of available RS data. Visual forms of representation such as classified satellite images, maps, graphs and tables with obtained statistical information effectively summarise information and present it in an interpretable form, which enables researchers to highlight important zones of endangered coastal regions on maps. The use of such data in coastal monitoring supports a high level of complexity and operability of mapping due to technical advancements in GIS and progress in programming, including using AI and ML algorithm. Using scripting techniques of GRASS GIS enhanced through ML and AI algorithms enabled us to automate and improve manual mapping in order to increase the precision and quality of images and to contribute to the monitoring of coastal land use types in southern Australia.

The challenge of future studies is to integrate and revitalise diverse sources of information for a comprehensive analysis of coastal zones. Hence, in further works that perform similar analyses of coastal areas, the integrated methods can bring research to a principally novel level. Namely, ML-supported RS data processing by GIS can help explore coastal landscape dynamics. When applied to environmental monitoring of coasts that have been affected by climate hazards or erosion, such data integration promises effective tools for decision-making. Hence, future studies will consider the smooth integration of data and methods, which are notable for the multi-disciplinary coastal monitoring supported by Earth observation data and spatial analysis.

To conclude, coastal monitoring is a systematic research area with the goal of making decisions based on the diversity of multi-format data and advanced tools for their processing. Thus, the input data can be included in various forms such as RS satellite images, cartographic data, computational tables based on ecological surveys, experimental evaluations or user opinion surveys for coastal environmental monitoring. The advantages, benefits and usage conditions for such methods and tools for novel research directions in coastal mapping should be considered and applied in similar works. Hence, as demonstrated in this study, using modern technologies of satellite image processing, statistical GIS analysis and programming plays a crucial role in driving environmental modelling towards the advanced level of research performed by a modern GIS.

Funding: The publication was funded by the Editorial Office of Journal of Marine Science and Engineering (JMSE), Multidisciplinary Digital Publishing Institute (MDPI) and Institutional Open Access Program (IOAP) participating institution University of Salzburg.

Institutional Review Board Statement: Not applicable.

Informed Consent Statement: Not applicable.

Data Availability Statement: The programming scripts used for AI- and ML-based remote sensing data processing and the reports on classification are available in the GitHub repository of the author: https://github.com/paulinelemenkova/Australia_GRASS_GIS_AI_ML (accessed on 18 July 2024).

Acknowledgments: The author thanks the reviewers for reading and review of this manuscript.

Conflicts of Interest: The author declares no conflicts of interest.

Abbreviations

The following abbreviations are used in this manuscript:

AI	Artificial Intelligence
ANN	Artificial Neural Network
DN	Digital Number
DOS	Dark Object Subtraction
EO	Earth Observation
GCP	Ground Control Point
GEBCO	General Bathymetric Chart of the Oceans
GMT	Generic Mapping Tools
GRASS	Geographic Resources Analysis Support System
GIS	Geographic Information System
Landsat OLI/TIRS	Landsat Operational Land Imager and Thermal Infrared Sensor
ML	Machine Learning
MLP	Multilayer Perceptron
MODIS	Moderate Resolution Imaging Spectroradiometer
NIR	Near Infrared
RF	Random Forest
R&D	Research and Development
RS	Remote Sensing
SPOT	Satellite Pour l'Observation de la Terre
SVM	Support Vector Machine
SWIR	Shortwave Infrared
USGS	United States Geological Survey
UTM	Universal Transverse Mercator
WGS84	World Geodetic System 84
WRS	Worldwide Reference System

Appendix A. Initial Means for Each Band

Table A1. Initial mean values for pixels in each band assigned to target land cover types for images from 2013 before the iterative classification process.

Class	Initial Mean Values for Multispectral Bands of Landsat						
	1—Coastal Aerosol	2—Blue	3—Green	4—Red	5—NIR	6—SWIR-1	7—SWIR-2
1	7944.36	8195.91	8742.78	8861.72	12,337.5	12,337.4	10,304.5
2	8119.86	8408.03	9026.45	9267.03	12,909.9	13,277	11,008.4
3	8295.36	8620.15	9310.11	9672.33	13,482.2	14,216.6	11,712.2
4	8470.86	8832.27	9593.77	10,077.6	14,054.6	15,156.2	12,416.1
5	8646.36	9044.38	9877.44	10,482.9	14,627	16,095.8	13,120
6	8821.86	9256.5	10,161.1	10,888.3	15,199.4	17,035.4	13,823.8
7	8997.36	9468.62	10,444.8	11,293.6	15,771.7	17,975	14,527.7
8	9172.86	9680.74	10,728.4	11,698.9	16,344.1	18,914.6	15,231.5
9	9348.36	9892.86	11,012.1	12,104.2	16,916.5	19,854.2	15,935.4
10	9523.86	10,105	11,295.8	12,509.5	17,488.8	20,793.8	16,639.3

Table A2. Initial mean values for pixels in each band assigned to target land cover types for images from 2015 before the iterative classification process.

Class	Initial Mean Values for Multispectral Bands of Landsat						
	1—Coastal Aerosol	2—Blue	3—Green	4—Red	5—NIR	6—SWIR-1	7—SWIR-2
1	7964.53	8167.16	8635.84	8723.91	12,003.5	11,922.3	10,077.8
2	8143.64	8371.91	8901.87	9095.84	12,597.6	12,891.5	10,824.4
3	8322.74	8576.66	9167.9	9467.76	13,191.7	13,860.6	11,571
4	8501.84	8781.41	9433.92	9839.69	13,785.8	14,829.8	12,317.6
5	8680.94	8986.16	9699.95	10,211.6	14,379.8	15,798.9	13,064.2
6	8860.04	9190.91	9965.98	10,583.5	14,973.9	16,768.1	13,810.8
7	9039.15	9395.66	10,232	10,955.5	15,568	17,737.2	14,557.5
8	9218.25	9600.41	10,498	11,327.4	16,162.1	18,706.4	15,304.1
9	9397.35	9805.16	10,764.1	11,699.3	16,756.2	19,675.5	16,050.7
10	9576.45	10,009.9	11,030.1	12,071.2	17,350.2	20,644.7	16,797.3

Table A3. Initial mean values for pixels in each band assigned to target land cover types for images from 2017 before the iterative classification process.

Class	Initial Mean Values for Multispectral Bands of Landsat						
	1—Coastal Aerosol	2—Blue	3—Green	4—Red	5—NIR	6—SWIR-1	7—SWIR-2
1	7956.33	8207.65	8763.65	8860.93	12,306	11,946.7	10,001.2
2	8117.93	8401.46	9023.47	9249.65	12,895.4	12,888	10,677.9
3	8279.53	8595.27	9283.28	9638.37	13,484.7	13,829.4	11,354.6
4	8441.13	8789.08	9543.09	10,027.1	14,074.1	14,770.7	12,031.3
5	8602.73	8982.89	9802.91	10,415.8	14,663.4	15,712	12,708
6	8764.32	9176.7	10,062.7	10,804.5	15,252.8	16,653.4	13,384.7
7	8925.92	9370.51	10,322.5	11,193.3	15,842.1	17,594.7	14,061.4
8	9087.52	9564.32	10,582.3	11,582	16,431.5	18,536.1	14,738.1
9	9249.12	9758.14	10,842.2	11,970.7	17,020.8	19,477.4	15,414.8
10	9410.72	9951.95	11,102	12,359.4	17,610.2	20,418.7	16,091.6

Table A4. Initial mean values for pixels in each band assigned to target land cover types for images from 2024 before the iterative classification process.

Class	Initial Mean Values for Multispectral Bands of Landsat						
	1—Coastal Aerosol	2—Blue	3—Green	4—Red	5—NIR	6—SWIR-1	7—SWIR-2
1	7883.17	8161.79	8731.22	8868.39	12,420.6	11,749.3	9919.64
2	8066.83	8374.7	9010.16	9289.44	13,074.4	12,751.4	10,645.2
3	8250.49	8587.61	9289.1	9710.5	13,728.3	13,753.5	11,370.7
4	8434.15	8800.53	9568.04	10,131.5	14,382.2	14,755.5	12,096.3
5	8617.81	9013.44	9846.97	10,552.6	15,036	15,757.6	12,821.8
6	8801.47	9226.35	10,125.9	10,973.7	15,689.9	16,759.6	13,547.4
7	8985.13	9439.26	10,404.9	11,394.7	16,343.7	17,761.7	14,272.9
8	9168.79	9652.17	10,683.8	11,815.8	16,997.6	18,763.8	14,998.4
9	9352.45	9865.08	10,962.7	12,236.8	17,651.4	19,765.8	15,724
10	9536.11	10,078	11,241.7	12,657.9	18,305.3	20,767.9	16,449.5

Appendix B. Iterative Cycles of Image Classification

Table A5. Iterative process of pixels' assignment to target classes during image classification: 2013.

2013	Pixels' Distribution by Categories of Land Cover Classes										
	Points Stable	1	2	3	4	5	6	7	8	9	10
Iteration 1	79.91%	747	855	508	460	478	595	688	802	1014	897
Iteration 2	88.69%	558	897	671	456	477	594	683	861	1075	772
Iteration 3	90.81%	513	801	806	491	449	603	693	893	1108	687
Iteration 4	93.02%	510	733	867	506	448	618	701	910	1129	622
Iteration 5	95.30%	508	690	912	515	417	641	727	910	1145	579
Iteration 6	96.39%	507	671	924	531	398	668	698	948	1149	550
Iteration 7	97.30%	507	655	924	556	387	701	658	966	1163	527
Iteration 8	97.90%	507	646	905	585	381	734	613	987	1175	511
Iteration 9	98.27%	507	638	887	617	378	748	584	1004	1175	506

Table A6. Iterative process of pixels' assignment to target classes during image classification: 2015.

2015	Pixels' Distribution by Categories of Land Cover Classes										
	Points Stable	**1**	**2**	**3**	**4**	**5**	**6**	**7**	8	**9**	**10**
Iteration 1	77.04%	766	831	451	500	490	594	722	763	1028	860
Iteration 2	88.08%	627	815	610	509	470	609	708	848	1094	715
Iteration 3	89.31%	584	751	685	567	474	591	711	912	1122	608
Iteration 4	91.53%	575	693	760	585	440	629	717	939	1144	523
Iteration 5	93.52%	573	663	791	612	396	667	707	979	1169	448
Iteration 6	96.20%	573	646	787	636	383	719	664	994	1203	400
Iteration 7	97.36%	571	636	776	666	385	750	633	1006	1223	359
Iteration 8	97.79%	569	622	779	688	386	776	603	1021	1236	325
Iteration 9	98.34%	568	615	781	703	391	796	582	1026	1245	298

Table A7. Iterative process of pixels' assignment to target classes during image classification: 2017.

2017	Pixels' Distribution by Categories of Land Cover Classes										
	Points Stable	**1**	**2**	**3**	**4**	**5**	**6**	**7**	8	**9**	**10**
Iteration 1	74.38%	695	882	485	429	448	618	766	849	1079	760
Iteration 2	91.54%	602	844	621	429	456	599	775	930	1100	655
Iteration 3	91.93%	585	772	687	445	479	598	780	978	1094	593
Iteration 4	93.21%	583	737	704	447	500	588	809	1006	1093	544
Iteration 5	95.31%	583	723	707	435	528	588	818	1049	1071	509
Iteration 6	96.38%	583	724	699	429	534	601	813	1086	1061	481
Iteration 7	96.41%	583	722	688	433	531	622	806	1106	1066	454
Iteration 8	96.36%	583	722	669	446	533	656	785	1105	1083	429
Iteration 9	96.65%	583	723	643	468	531	691	771	1089	1094	418
Iteration 10	96.82%	582	726	621	486	538	723	739	1074	1113	409
Iteration 11	97.10%	582	724	586	524	537	757	708	1060	1129	404
Iteration 12	97.39%	582	704	552	582	536	786	682	1047	1139	401
Iteration 13	97.62%	581	683	523	633	536	816	652	1044	1142	401
Iteration 14	98.12%	581	673	494	674	534	836	629	1048	1140	402

Table A8. Iterative process of pixels' assignment to target classes during image classification: 2024.

2024	Pixels' Distribution by Categories of Land Cover Classes										
	Points Stable	**1**	**2**	**3**	**4**	**5**	**6**	**7**	8	**9**	**10**
Iteration 1	78.77%	763	1016	519	447	436	517	673	772	1086	988
Iteration 2	89.39%	637	969	688	458	430	523	665	845	1148	854
Iteration 3	90.56%	616	845	794	491	458	493	685	913	1160	762
Iteration 4	93.17%	612	772	854	465	477	523	686	967	1160	701
Iteration 5	95.08%	611	734	885	436	477	561	688	1000	1161	664
Iteration 6	96.16%	609	706	897	429	469	598	702	989	1173	645
Iteration 7	97.06%	609	685	907	421	460	646	714	952	1193	630
Iteration 8	97.73%	609	675	907	415	452	687	739	910	1197	626
Iteration 9	98.41%	609	670	902	411	456	712	770	860	1204	623

References

1. Agate, J.; Ballinger, R.; Ward, R.D. Satellite remote sensing can provide semi-automated monitoring to aid coastal decision-making. *Estuar. Coast. Shelf Sci.* **2024**, *298*, 108639. [CrossRef]
2. Lemenkova, P. Exploitation d'images satellitaires Landsat de la région du Cap (Afrique du Sud) pour le calcul et la cartographie d'indices de végétation à l'aide du logiciel GRASS GIS. *Physio-Géo* **2024**, *20*, 113–129. [CrossRef]
3. Liu, S.; Kim, S.; Glamore, W.; Tamburic, B.; Johnson, F. Remote sensing of water colour in small southeastern Australian waterbodies. *J. Environ. Manag.* **2024**, *352*, 120096. [CrossRef] [PubMed]
4. Sheng, Z.; Ge, L.; Li, C.; Bai, T.; Liu, C.; Wu, Y.; Zhang, Q. Flood Assessment and Mapping Based on SAR and QUAV Vertical Remote Sensing Framework: A Case Study of 2022 Australia Moama Floods. In Proceedings of the IGARSS 2023—2023 IEEE International Geoscience and Remote Sensing Symposium, Pasadena, CA, USA, 16–21 July 2023; pp. 2548–2551. [CrossRef]
5. Yebra, M.; Quan, X.; Riaño, D.; Rozas Larraondo, P.; van Dijk, A.I.; Cary, G. Mapping Live Fuel Moisture Content and Flammability for Continental Australia Using Optical Remote Sensing. In Proceedings of the IGARSS 2018—2018 IEEE International Geoscience and Remote Sensing Symposium, Valencia, Spain, 22–27 July 2018; pp. 5903–5906. [CrossRef]

6. Caruso, A.S.; Clarke, K.D.; Tiddy, C.J.; Lewis, M.M. Integrating Hyperspectral and Radiometric Remote Sensing, Spatial Topographic Analysis and Surface Geochemistry to Assist Mineral Exploration in Southern Australia. In Proceedings of the IGARSS 2019—2019 IEEE International Geoscience and Remote Sensing Symposium, Yokohama, Japan, 28 July–2 August 2019; pp. 6783–6786. [CrossRef]
7. McCarroll, R.J.; Kennedy, D.M.; Liu, J.; Allan, B.; Ierodiaconou, D. Design and application of coastal erosion indicators using satellite and drone data for a regional monitoring program. *Ocean Coast. Manag.* **2024**, *253*, 107146. [CrossRef]
8. Munroe, S.E.M.; Guerin, G.R.; McInerney, F.A.; Martín-Forés, I.; Welti, N.; Farrell, M.; Atkins, R.; Sparrow, B. A vegetation carbon isoscape for Australia built by combining continental-scale field surveys with remote sensing. *Landsc. Ecol.* **2022**, *37*, 1987–2006. [CrossRef]
9. Morgan, G.R.; Hodgson, M.E.; Wang, C.; Schill, S.R. Unmanned aerial remote sensing of coastal vegetation: A review. *Ann. GIS* **2022**, *28*, 385–399. [CrossRef]
10. Traganos, D.; Reinartz, P. Machine learning-based retrieval of benthic reflectance and Posidonia oceanica seagrass extent using a semi-analytical inversion of Sentinel-2 satellite data. *Int. J. Remote Sens.* **2018**, *39*, 9428–9452. [CrossRef]
11. Zhu, L.; Cui, T.; Runa, A.; Pan, X.; Zhao, W.; Xiang, J.; Cao, M. Robust remote sensing retrieval of key eutrophication indicators in coastal waters based on explainable machine learning. *ISPRS J. Photogramm. Remote Sens.* **2024**, *211*, 262–280. [CrossRef]
12. Munizaga, J.; García, M.; Ureta, F.; Novoa, V.; Rojas, O.; Rojas, C. Mapping Coastal Wetlands Using Satellite Imagery and Machine Learning in a Highly Urbanized Landscape. *Sustainability* **2022**, *14*, 5700. [CrossRef]
13. Lemenkova, P. A GRASS GIS Scripting Framework for Monitoring Changes in the Ephemeral Salt Lakes of Chotts Melrhir and Merouane, Algeria. *Appl. Syst. Innov.* **2023**, *6*, 61. [CrossRef]
14. Zhu, X.; Guo, H.; Huang, J.J.; Tian, S.; Xu, W.; Mai, Y. An ensemble machine learning model for water quality estimation in coastal area based on remote sensing imagery. *J. Environ. Manag.* **2022**, *323*, 116187. [CrossRef] [PubMed]
15. Lemenkova, P. Monitoring Seasonal Fluctuations in Saline Lakes of Tunisia Using Earth Observation Data Processed by GRASS GIS. *Land* **2023**, *12*, 1995. [CrossRef]
16. Kim, Y.H.; Im, J.; Ha, H.K.; Choi, J.K.; Ha, S. Machine learning approaches to coastal water quality monitoring using GOCI satellite data. *GISci. Remote Sens.* **2014**, *51*, 158–174. [CrossRef]
17. McAllister, E.; Payo, A.; Novellino, A.; Dolphin, T.; Medina-Lopez, E. Multispectral satellite imagery and machine learning for the extraction of shoreline indicators. *Coast. Eng.* **2022**, *174*, 104102. [CrossRef]
18. Murray, A.G.; Parslow, J.S.; Walker, S.J.; Waring, J.R. The implementation of the ecosystem module of a coastal environmental model: Port Phillip Bay, Australia. *Environ. Model. Softw.* **2000**, *15*, 357–372. [CrossRef]
19. Coutts, A.M.; Harris, R.J.; Phan, T.; Livesley, S.J.; Williams, N.S.; Tapper, N.J. Thermal infrared remote sensing of urban heat: Hotspots, vegetation, and an assessment of techniques for use in urban planning. *Remote Sens. Environ.* **2016**, *186*, 637–651. [CrossRef]
20. Bishop-Taylor, R.; Nanson, R.; Sagar, S.; Lymburner, L. Mapping Australia's dynamic coastline at mean sea level using three decades of Landsat imagery. *Remote Sens. Environ.* **2021**, *267*, 112734. [CrossRef]
21. Antos, M.J.; Ehmke, G.C.; Tzaros, C.L.; Weston, M.A. Unauthorised human use of an urban coastal wetland sanctuary: Current and future patterns. *Landsc. Urban Plan.* **2007**, *80*, 173–183. [CrossRef]
22. Abuzar, M.; Whitfield, D.; McAllister, A.; Lamb, G.; Sheffield, K.; O'Connell, M. Satellite remote sensing of crop water use in an irrigation area of south-east Australia. In Proceedings of the 2013 IEEE International Geoscience and Remote Sensing Symposium—IGARSS, Melbourne, VIC, Australia, 21–26 July 2013; pp. 3269–3272. [CrossRef]
23. Weston, M.A.; Antos, M.J.; Tzaros, C.L. Sand pads: A promising technique to quantify human visitation into nature conservation areas. *Landsc. Urban Plan.* **2009**, *89*, 98–104. [CrossRef]
24. Leia Howes, C.S.; Parsons, E.C.M. Ineffectiveness of a marine sanctuary zone to protect burrunan dolphins (Tursiops australis sp.nov.) from commercial tourism in Port Phillip Bay, Australia. *J. Ecotourism* **2012**, *11*, 188–201. [CrossRef]
25. Glenn, E.P.; Doody, T.M.; Guerschman, J.P.; Huete, A.R.; King, E.A.; McVicar, T.R.; Van Dijk, A.I.J.M.; Van Niel, T.G.; Yebra, M.; Zhang, Y. Actual evapotranspiration estimation by ground and remote sensing methods: The Australian experience. *Hydrol. Process.* **2011**, *25*, 4103–4116. [CrossRef]
26. Lemenkova, P. Evapotranspiration, vapour pressure and climatic water deficit in Ethiopia mapped using GMT and TerraClimate dataset. *J. Water Land Dev.* **2022**, *54*, 201–209. [CrossRef]
27. Costa, M.D.P.; Wartman, M.; Macreadie, P.I.; Ferns, L.W.; Holden, R.L.; Ierodiaconou, D.; MacDonald, K.J.; Mazor, T.K.; Morris, R.; Nicholson, E.; et al. Spatially explicit ecosystem accounts for coastal wetland restoration. *Ecosyst. Serv.* **2024**, *65*, 101574. [CrossRef]
28. Lemenkova, P. Landscape Fragmentation and Deforestation in Sierra Leone, West Africa, Analysed Using Satellite Images. *Transylv. Rev. Syst. Ecol. Res.* **2024**, *26*, 13–26. [CrossRef]
29. Gao, J.; Kennedy, D.M.; McSweeney, S. Decadal changes in vegetation cover within coastal dunes at the regional scale in Victoria, SE Australia. *J. Environ. Manag.* **2024**, *351*, 119622. [CrossRef] [PubMed]
30. Vasquez, J.; Acevedo-Barrios, R.; Miranda-Castro, W.; Guerrero, M.; Meneses-Ospina, L. Determining Changes in Mangrove Cover Using Remote Sensing with Landsat Images: A Review. *Water Air Soil Pollut.* **2023**, *235*, 18. [CrossRef]
31. Masria, A. Bridging coastal challenges: The role of remote sensing and future research. *Reg. Stud. Mar. Sci.* **2024**, *73*, 103502. [CrossRef]

32. Blackford, J.; Radford, P. A structure and methodology for marine ecosystem modelling. *Neth. J. Sea Res.* **1995**, *33*, 247–260. [CrossRef]
33. Whig, P.; Bhatia, A.B.; Nadikatu, R.R.; Alkali, Y.; Sharma, P. GIS and Remote Sensing Application for Vegetation Mapping. In *Geo-Environmental Hazards Using AI-Enabled Geospatial Techniques and Earth Observation Systems*; Springer Nature Switzerland: Cham, Switzerland, 2024; pp. 17–39. [CrossRef]
34. Rolim, S.B.A.; Veettil, B.K.; Vieiro, A.P.; Kessler, A.B.; Gonzatti, C. Remote sensing for mapping algal blooms in freshwater lakes: A review. *Environ. Sci. Pollut. Res.* **2023**, *30*, 19602–19616. [CrossRef]
35. Bugnot, A.; Lyons, M.; Scanes, P.; Clark, G.; Fyfe, S.; Lewis, A.; Johnston, E. A novel framework for the use of remote sensing for monitoring catchments at continental scales. *J. Environ. Manag.* **2018**, *217*, 939–950. [CrossRef]
36. Park, S.; Song, A. Shoreline Change Analysis with Deep Learning Semantic Segmentation Using Remote Sensing and GIS Data. *KSCE J. Civ. Eng.* **2024**, *28*, 928–938. [CrossRef]
37. Mary, S.R.; Pachar, S.; Srivastava, P.K.; Malik, M.; Sharma, A.; Almutiri, T.G.; Atal, Z. Deep Learning Model for the Image Fusion and Accurate Classification of Remote Sensing Images. *Comput. Intell. Neurosci.* **2022**, *2022*, 2668567. [CrossRef]
38. Lemenkova, P. Handling Dataset with Geophysical and Geological Variables on the Bolivian Andes by the GMT Scripts. *Data* **2022**, *7*, 74. [CrossRef]
39. Lemenkova, P. Mapping submarine geomorphology of the Philippine and Mariana trenches by an automated approach using GMT scripts. *Proc. Latv. Acad. Sci. Sect. B. Nat. Exact. Appl. Sci.* **2022**, *76*, 258–266. [CrossRef]
40. Hafeez, S.; Wong, M.S.; Ho, H.C.; Nazeer, M.; Nichol, J.; Abbas, S.; Tang, D.; Lee, K.H.; Pun, L. Comparison of Machine Learning Algorithms for Retrieval of Water Quality Indicators in Case-II Waters: A Case Study of Hong Kong. *Remote Sens.* **2019**, *11*, 617. [CrossRef]
41. Lemenkova, P. Mapping Ghana by GMT and R scripting: Advanced cartographic approaches to visualize correlations between the topography, climate and environmental setting. *Adv. Geod. Geoinf.* **2022**, *71*, 1–20. [CrossRef]
42. Turnbull, A.; Soto-Berelov, M.; Coote, M. Delineation and Classification of Wetlands in the Northern Jarrah Forest, Western Australia Using Remote Sensing and Machine Learning. *Wetlands* **2024**, *44*, 52. [CrossRef]
43. Lemenkova, P. Using open-source software GRASS GIS for analysis of the environmental patterns in Lake Chad, Central Africa. *Die Bodenkultur J. Land Manag. Food Environ.* **2023**, *74*, 49–64. [CrossRef]
44. Cao, Q.; Yu, G.; Qiao, Z. Application and recent progress of inland water monitoring using remote sensing techniques. *Environ. Monit. Assess.* **2022**, *195*, 125. [CrossRef]
45. Lemenkova, P. Mapping Climate Parameters over the Territory of Botswana Using GMT and Gridded Surface Data from TerraClimate. *ISPRS Int. J. Geo-Inf.* **2022**, *11*, 473. [CrossRef]
46. Australian Bureau of Statistics. National, State and Territory Population. Available online: https://www.abs.gov.au/statistics/people/population/national-state-and-territory-population/latest-release (accessed on 20 June 2024).
47. Liao, J.; Zhang, D.; Su, S.; Liang, S.; Du, J.; Yu, W.; Ma, Z.; Chen, B.; Hu, W. Coastal habitat quality assessment and mapping in the terrestrial-marine continuum: Simulating effects of coastal management decisions. *Ecol. Indic.* **2023**, *156*, 111158. [CrossRef]
48. Huang, B.; Young, M.A.; Carnell, P.E.; Conron, S.; Ierodiaconou, D.; Macreadie, P.I.; Nicholson, E. Quantifying welfare gains of coastal and estuarine ecosystem rehabilitation for recreational fisheries. *Sci. Total Environ.* **2020**, *710*, 134680. [CrossRef] [PubMed]
49. Holdgate, G.R.; Geurin, B.; Wallace, M.W.; Gallagher, S.J. Marine geology of Port Phillip, Victoria. *Aust. J. Earth Sci.* **2001**, *48*, 439–455. [CrossRef]
50. Longmore, A.R.; Cowdell, R.A.; Flint, R. *Nutrient Status of the Water in Port Phillip Bay*; Port Phillip Bay Environmental Study; CSIRO: Canberra, Australia, 1996.
51. Jenkins, G.P.; Coleman, R.A.; Barrow, J.S.; Morrongiello, J.R. Environmental drivers of fish population dynamics in an estuarine ecosystem of south-eastern Australia. *Fish. Manag. Ecol.* **2022**, *29*, 693–707. [CrossRef]
52. Weston, M.A.; Ekanayake, K.B.; Lomas, S.; Glover, H.K.; Mead, R.E.; Cribbin, A.; Tan, L.X.L.; Whisson, D.A.; Maguire, G.S.; Cardilini, A.P.A. Case studies of motion-sensing cameras to study clutch survival and fate of real and artificial ground-nests in Australia. *Bird Study* **2017**, *64*, 476–491. [CrossRef]
53. Harris, G. *Port Phillip Bay Environmental Study*; CSIRO Publishing: Canberra, Australia, 1996.
54. Boon, P.I.; Allen, T.; Carr, G.; Frood, D.; Harty, C.; Mcmahon, A.; Mathews, S.; Rosengren, N.; Sinclair, S.; White, M.; et al. Coastal wetlands of Victoria, south-eastern Australia: Providing the inventory and condition information needed for their effective management and conservation. *Aquat. Conserv. Mar. Freshw. Ecosyst.* **2015**, *25*, 454–479. [CrossRef]
55. Dobbie, M.F. Typing Colonial Perceptions of Carrum Carrum Swamp: The Expected and the Surprising. *Land* **2022**, *11*, 311. [CrossRef]
56. Weston, M.A.; Tzaros, C.L.; Antos, M.J. Awareness of wetlands and their conservation value among students at a primary school in Victoria, Australia. *Ecol. Manag. Restor.* **2006**, *7*, 223–226. [CrossRef]
57. Tran, H.Q.; Provis, D.; Babanin, A.V. Hydrodynamic Climate of Port Phillip Bay. *J. Mar. Sci. Eng.* **2021**, *9*, 898. [CrossRef]
58. Jackson, M.V.; Woodworth, B.K.; Bush, R.; Clemens, R.S.; Fuller, R.A.; Garnett, S.T.; Martine Maron, A.L.; Purnell, C.; Rogers, D.I.; Amano, T. Widespread use of artificial habitats by shorebirds in Australia. *Emu—Austral Ornithol.* **2021**, *121*, 187–197. [CrossRef]
59. Fulton, E.A.; Smith, A.D.M. Lessons learnt from a comparison of three ecosystem models for Port Phillip Bay, Australia. *Afr. J. Mar. Sci.* **2004**, *26*, 219–243. [CrossRef]

60. Phillips, D.; Richardson, B.; Murray, A.; Fabris, J. Trace metals, organochlorines and hydrocarbons in Port Phillip Bay, Victoria: A historical review. *Mar. Pollut. Bull.* **1992**, *25*, 200–217. [CrossRef]
61. Currie, D.R.; Parry, G.D. Changes to benthic communities over 20 years in Port Phillip Bay, Victoria, Australia. *Mar. Pollut. Bull.* **1999**, *38*, 36–43. [CrossRef]
62. Lever, J.; Brkljača, R.; Kraft, G.; Urban, S. Natural Products of Marine Macroalgae from South Eastern Australia, with Emphasis on the Port Phillip Bay and Heads Regions of Victoria. *Mar. Drugs* **2020**, *18*, 142. [CrossRef]
63. Roelfsema, C.; Dennison, B.; Phinn, S.; Dekker, A.; Brando, V. Remote sensing of a cyanobacterial bloom (Lyngbya majuscula) in Moreton Bay, Australia. In Proceedings of the IGARSS 2001. Scanning the Present and Resolving the Future. Proceedings. IEEE 2001 International Geoscience and Remote Sensing Symposium (Cat. No.01CH37217), Sydney, NSW, Australia, 9–13 July 2001; Volume 2, pp. 613–615. [CrossRef]
64. Jung, C.A.; Dwyer, P.D.; Minnegal, M.; Swearer, S.E. Perceptions of environmental change over more than six decades in two groups of people interacting with the environment of Port Phillip Bay, Australia. *Ocean Coast. Manag.* **2011**, *54*, 93–99. [CrossRef]
65. Vapnik, V. An overview of statistical learning theory. *IEEE Trans. Neural Netw.* **1999**, *10*, 988–999. [CrossRef]
66. Port Phillip & Western Port Regional Catchment Strategy. Victoria's Regional Catchment Strategies. Available online: https://portphillipwesternport.rcs.vic.gov.au/ (accessed on 21 June 2024).

Disclaimer/Publisher's Note: The statements, opinions and data contained in all publications are solely those of the individual author(s) and contributor(s) and not of MDPI and/or the editor(s). MDPI and/or the editor(s) disclaim responsibility for any injury to people or property resulting from any ideas, methods, instructions or products referred to in the content.